Received: 12 August 2024 | Revised: 25 September 2024 | Accepted: 26 September 2024

DOI: 10.1002/eom2.12492

EcoMat FUNCTIONAL MATERIALS FOR GREEN ENERGY AND ENVIRONMENT WILEY

REVIEW

Pt and Pt-group transition metal 0D vacancy ordered halide perovskites: A review

Huilong Liu[1] | **Shubhra Bansal**[1,2]

[1]School of Mechanical Engineering, Purdue University, West Lafayette, Indiana, USA

[2]School of Materials Engineering, Purdue University, West Lafayette, Indiana, USA

Correspondence
Shubhra Bansal, School of Mechanical Engineering, Purdue University, 205 Gates Rd, West Lafayette, IN 47906, USA.
Email: bansal91@purdue.edu

Funding information
National Science Foundation, Grant/Award Number: 2046944

Abstract

Lead halide perovskites (LHPs), have attracted considerable attention across various applications owing to their exceptional optoelectronic properties. However, the main challenge hindering the broad adoption of lead halide perovskites lies in their stability and toxicity. In this review, we summarize the outstanding properties of platinum (Pt) halide perovskites, with a particular focus on the stability and applications of Cs_2PtI_6 and its derivatives. Cs_2PtI_6 has shown promising efficiency for photovoltaic devices, as well as photoelectrochemical water splitting with stable behavior in acid or basic conditions. Cs_2PtI_6 also shows promise in gas sensing and thermoelectric devices. The emergence of 2D Pt (II) halide perovskites opens up new avenues for environmentally friendly materials for photonic and optoelectronic devices like room temperature phosphoresce and triplet-triplet annihilation (TTA) based up-conversion.

KEYWORDS

lead-free halide perovskite, metal halide perovskites, photoelectronic chemistry, photovoltaic, transition metal

1 | INTRODUCTION

In recent decades, lead-halide perovskites (LHPs) have emerged as a prominent class of materials due to their advantageous properties, including low-temperature processability and exceptional optoelectronic characteristics such as tunable and broadband light absorption, high extinction coefficient, long carrier lifetime, and defect tolerance.[1–5] While LHPs have demonstrated significant promise in applications like light emitting diodes (LEDs), photocatalysis, detectors, and photovoltaics (PV),[6–10] their commercial potential remains limited due to presence of toxic lead and limited stability.[10–14] The pursuit of non-toxic metal halide perovskites (MHPs) that retain the excellent properties of LHPs is crucial. Over the past years, considerable efforts have been directed towards substitution of Pb with elements such as tin (Sn), germanium (Ge), bismuth (Bi), antimony (Sb), and silver (Ag) to create Pb-free metal halide perovskites.[15–17] Beyond these emerging alternatives, Pt as the transition group metal has also been demonstrated in 0D perovskites.

In 2020, our research group successfully synthesized vacancy-ordered double perovskite Cs_2PtI_6 and utilized it as a photo-absorber in thin-film solar cells.[17] Since then, numerous experimental and theoretical investigations into platinum halide perovskites have emerged.[18–32] Platinum can exist in Pt^{2+} and Pt^{4+} oxidation states, however, the traditional 3D perovskite $APtX_3$ (A = MA, Cs; X = Cl, Br, and I), is structurally unstable due to

limitations imposed by lattice parameters (Goldschmidt and Bartel tolerance factors, and the factor of octahedra).[33,34] Consequently, existing studies on platinum halide perovskites have mainly focused on 0D vacancy ordered double perovskite Cs_2PtI_6 and its analogues with ionic substitutions in the A site and X site of A_2PtX_6 (e.g., A = Cs, K, In, Tl, Rb; X = Cl, Br, and I).

In the subsequent sections, we provide a review of the properties and applications of Pt halide vacancy-ordered double perovskites, covering aspects such as biocompatibility, stability, electronic structure, thermoelectric figure of merit, and their exceptional potential for applications such as water splitting. A brief overview is also provided on our recent discovery of stable 2D-Pt halide perovskites that exhibit generation of triplet excitons via singlet-triplet intersystem crossing and phosphorescence and show significant potential for triplet-triplet annihilation (TTA) up-conversion.

2 | Pt-BASED VACANCY ORDERED DOUBLE PEROVSKITES

2.1 | Biocompatibility

While lead halide perovskites exhibit numerous advantages in various applications owing to their exceptional optoelectronic properties, they are still hindered from widespread commercialization due to significant environmental risks associated with lead toxicity and stability issues. For instance, lead halide perovskites used in photovoltaic panels are susceptible to UV light, water, moisture, and thermal stress, leading to the formation of water-soluble Pb-halide salts.[10,14] The dissolved lead poses high bioavailability risks and a variety of toxicity to plants, animals, human beings, and microbes.[13,35,36] Accumulation of lead in the human body, particularly in femoral bone stores, can result in adverse health effects such as renal dysfunction, reproductive system defects, and blood–brain barrier dysfunction.[13] In contrast, platinum exhibits excellent biocompatibility suitable for biomedical use, such as medical implants, drug delivery, and cancer therapy.[37,38] Shinde et al. explored the biocompatibility of Cs_2PtX_6 (X = Cl, Br, and I) vacancy ordered double perovskites and their interaction with *Shewanella oneidensis* MR-1 bacteria.[39] Cs_2PtX_6 did not affect the bacteria growth rate, and also *S. oneidensis* MR-1 bacteria did not degrade the vacancy ordered perovskite Cs_2PtX_6. The biocompatibility of Cs_2PtX_6 with the bacterium enables the design of biohybrid system, which can act as a platform to enable crucial redox reactions essential for environment, such as the conversion of carbon dioxide for sustainable fuel production.[39]

2.2 | Structure and composition

Cs_2PtI_6 crystallizes in face-centered cubic phase with $Fm\bar{3}m$ (no. 225) space group, and lattice constant of 11.37 Å.[40] Cs atoms occupy the 8c Wyckoff positions at coordinates (1/4, 1/4, 1/4), Pt located at the 4a Wyckoff positions with coordinates (0, 0, 0), and I atoms are situated at the 24e Wyckoff positions with coordinates (x, 0, 0), where x is approximately 0.20 (Figure 1A). Pt atoms occupy both the corners and face-center positions of the cube, and form $[PtI_6]^{2-}$ octahedra. The Pt—I interaction exhibits traits of covalent bonding, underscored by pronounced charge sharing in the Pt—I bond, attributable to a modest electronegativity difference of 0.38.[30] Cs atoms positioned within the octahedral cage physically bind with the $[PtI_6]^{2-}$ octahedra, with considerable ionic bond contribution between Cs and Pt/I. Through ion substitution of A site and/or X site, extensive experimental and theoretical investigations have also been conducted on the vacancy-ordered Pt halide double perovskites. Theoretical study by Abdeiaziz et al.[26] and Ye et al.[31] have predicted the structure of $Cs_2PtI_{6-y}Cl_y$, $Cs_2PtI_{6-y}Br_y$, $Cs_2PtBr_{6-y}Cl_y$ through X-site anion substitution, where halide mixed within the single $[PtX_6]^{2-}$ structure (Figure 1B). Hamdan et al. fabricated Cs_2PtX_6 (X = Cl, Br, and I) through hydrothermal method, all crystallizing in $Fm\bar{3}m$ space group.[19] A peak shift towards higher 2θ in the x-ray diffraction (XRD) pattern of Cs_2PtX_6 was observed as the halide (X) changed from iodide to bromide to chloride. (Figure 1C). This shift is ascribed to the smaller ionic radius of Cl (1.81 Å) relative to Br (1.96 Å) and I (2.2 Å), consistent with reported increases in lattice parameters (Cs_2PtCl_6: 10.19 Å, Cs_2PtBr_6: 10.67 Å, and Cs_2PtI_6: 11.37 Å). Furthermore, they investigated the tunability of mixed halides in $Cs_2PtCl_{6-x}Br_x$ by employing anion exchange techniques with Br salt solution, resulting in core–shell heterostructures where the particles surface is Br rich with the bulk containing Cl (Figure 1D). Notably, the anion exchange from the particle shell to the core produced two distinct types of octahedral structures ($[PtCl_6]^{2-}$ and $[PtBr_6]^{2-}$), as evidenced by the peak variations in XRD and Fourier transform infrared spectroscopy (FTIR) with respect to immersion time (Figure 1E,F), rather than mixed halides within a single $[PtX_6]^{2-}$ structure. Peng et al. reported the synthesis of ligand-free Cs_2PtBr_6 nanocrystals (NCs).[23] The process resulted in highly uniform and monodispersed NCs. These nanocrystals have an average diameter of 3.8 ± 0.4 nm and exhibited high crystallinity. The lattice spacing is 1.9 Å, which is consistent with the (440) plane of the Cs_2PtI_6 structure, which has a lattice parameter of 10.74 Å.

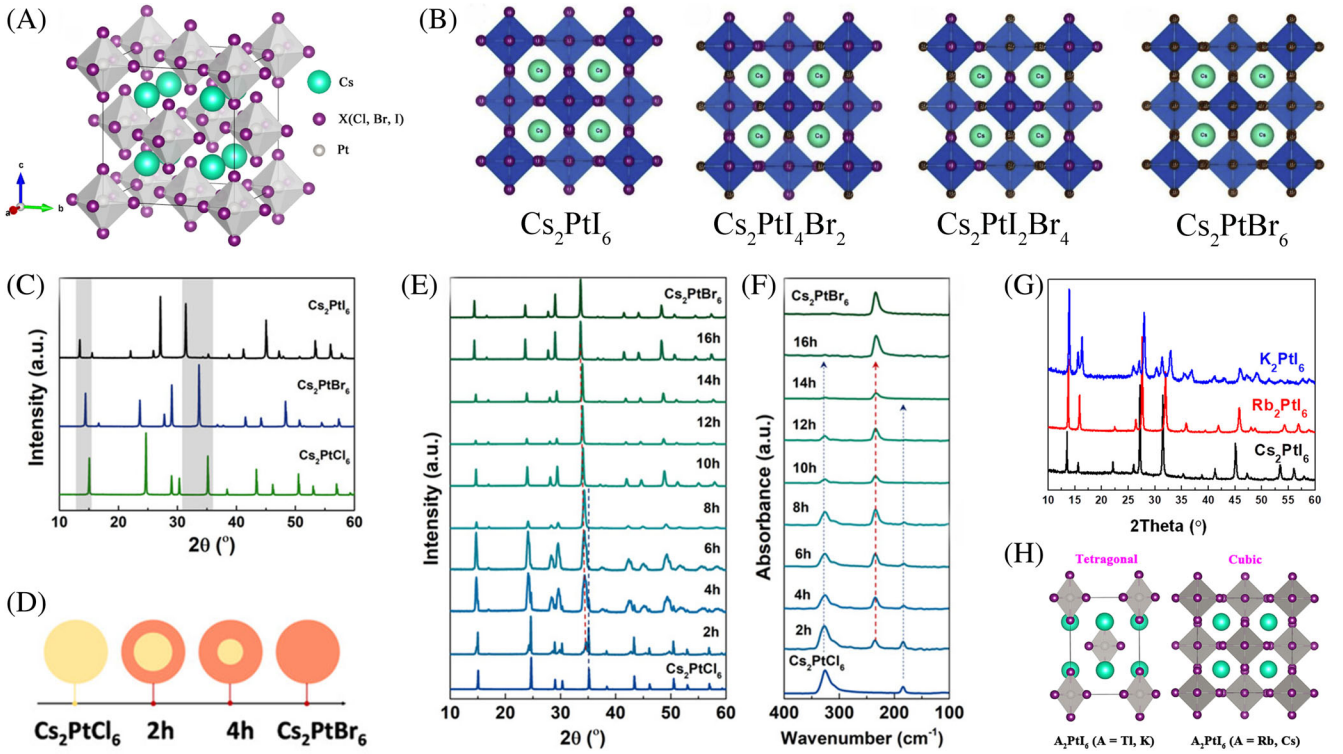

FIGURE 1 Structural properties. (A) Schematic crystal structure of Cs_2PtX_6 (X = Cl, Br, and I). Reproduced with permission: Copyright 2022, John Wiley and Sons.[31] (B) The crystal structures of Cs_2PtI_6, $Cs_2PtI_4Br_2$, $Cs_2PtI_2Br_4$, and Cs_2PtBr_6, respectively. Reproduced with permission: Copyright 2022, Elesvier.[26] (C) x-Ray crystallography (XRD) patterns of Cs_2PtI_6 (X = Cl^-, Br^-, and I^-). (D) Anion exchange mechanism of core–shell conversion of Cs_2PtCl_6 to Cs_2PtBr_6. (E) XRD patterns showing the shell conversion of Cs_2PtCl_6 to Cs_2PtBr_6. (F) FTIR peaks variation showing the shell conversion of Cs_2PtCl_6 to Cs_2PtBr_6. The (C)–(F) are reproduced with permission: Copyright 2022, John Wiley and Sons.[19] (G) x-Ray diffraction patterns of A_2PtI_6 (A = Cs^+, Rb^+, or K^+). Reproduced with permission: Copyright 2021, American Chemical Society.[21] (H) The tetragonal crystal structure of TI_2PtI_6, K_2PtI_6, and cubic crystal structure of Rb_2PtI_6, and Cs_2PtI_6, respectively. Reproduced with permission: Copyright 2022, Elsevier.[41]

Jayaraman et al. synthesized A_2PtI_6 (A = Cs^+, Rb^+, K^+) demonstrating A-site ion substitution.[21] Replacing Cs^+ (r_{Cs+} = 1.88 Å) into Rb^+ causes the XRD peaks to shift to higher 2θ values, attributed to the smaller ionic radius (r_{Rb+} = 1.72 Å) (Figure 1G). Despite this shift, the cubic phase of the material is retained. However, replacing the cation with K^+ (1.64 Å) leads to distortion of the $[PtI_6]^{2-}$ octahedra, with the diffraction pattern revealing a tetragonal crystal structure for K_2PtI_6. This indicates that A site could tune the crystal structure of vacancy-ordered perovskites. Although the A cation is not directly involved in the electronic band structure, it primarily interacts physically with the $[PtI_6]^{2-}$ octahedra. Theoretical investigation conducted by Sa et al. revealed a consistent conclusion: K_2PtI_6 is favored in tetragonal phase, whereas Rb_2PtI_6, Cs_2PtI_6 and In_2PtI_6 are demonstrated with cubic phase (Figure 1H).[41] The structure and lattice parameters of A_2PtX_6 double perovskites are summarized in Table 1.

2.3 | Thermal, chemical, and phase stability

Pb-based halide perovskites have demonstrated remarkable photovoltaic power conversion efficiency, however, device photostability, susceptibility to moisture and oxygen remain formidable challenge for successful integration into energy conversion systems.[20,42,43] Oxygen in the atmosphere tends to impede photogenerated electrons in conduction band, forming superoxide (O_2^-), followed by organic cation deprotonation process (e.g., methylammonium (MA) in organic–inorganic halide perovskite (e.g., $MAPbI_3$). Moisture can also induce material decomposition, even in dark leading to the formation of a hydrated phase.[44,45]

Inorganic double halide perovskite Cs_2PtX_6 stands out for its exceptional stability under ambient conditions and various pH aqueous media. Hamdan et al. observed negligible change in the XRD patterns of as-synthesized Cs_2PtI_6 stored under ambient conditions for a year, confirming its long-term ambient stability as shown in

TABLE 1 Structure and lattice parameters of A_2PtX_6 Pt halide double perovskites.

Compound	Lattice parameters (Å)	Structure	References
Cs_2PtI_6	11.37	Cubic	40
Cs_2PtI_6	6.56 for (220) plane	Cubic	18
Cs_2PtI_6	11.37	Cubic	32
Cs_2PtI_6	10.67	Cubic	32
Cs_2PtI_6	11.77	Cubic	41
Cs_2PtBr_6	10.74 (1.9; 440 surface)	Cubic	23
Cs_2PtCl_6	10.19	Cubic	32
Cs_2PtCl_6	10.19	Cubic	89
In_2PtCl_6	10.02, 10.18	Cubic	28
In_2PtBr_6	10.47	Cubic	28
In_2PtI_6	11.19	Cubic	28
Tl_2PtCl_6	10.07, 10.02	Cubic	28
Tl_2PtBr_6	10.53,10.49	Cubic	28
Tl_2PtI_6	11.26, 11.25	Cubic	28
Rb_2PtI_6	–	Cubic	21
Rb_2PtI_6	11.54	Cubic	41
K_2PtI_6	–	Tetragonal	21
K_2PtI_6	11.40	Cubic	41

Figure 2A.[20] Additionally, the Cs_2PtI_6 based solar cell prepared by Yang et al. retained 80% of PCE at 82.8°C up to 60 days in ambient conditions as well as in 100% relative humidity (RH), and UV-irradiation (Figure 2B).[22] Thermogravimetric analysis revealed exceptional thermal stability for Cs_2PtI_6 (Figure 2C), withstanding temperatures up to 364°C, surpassing Cs_2SnI_6 by over 100°C.[20] Despite their high photovoltaic efficiency, conventional halide perovskites suffer from poor stability in aqueous electrolyte media, which limits their application in electrochemical (EC) or photoelectrochemical (PEC) systems. Notably, Cs_2PtI_6 exhibited remarkable stability in aqueous electrolyte media (with no sign of decomposition when immersed in water for 40 days (Figure 2D),[22] remaining intact even under extremely acidic or basic conditions (pH 1–13) over 24 h, making it promising for EC or PEC applications.[20] Furthermore, Cs_2PtI_6 displayed stability through at least 100 electrochemical cycles and 6 h of H_2 production in aqueous solution at pH 1. Constant voltage measurements indicated over 12 h of PEC stability without performance degradation, even without surface protection or ligand modification.

The clues to the extraordinary stability of Cs_2PtI_6 can be found in many aspects: (1) its close proximity to ideal cubic crystal structure according to Goldschmidt tolerance factor $\tau = \frac{r_A + r_X}{\sqrt{2}(r_B + r_X)}$ ($0.89 < \tau < 1$ for cubic). The tolerance factor of Cs_2PtI_6 is 0.962, which is near 1, suggesting that Cs_2PtI_6 is stable as a symmetric cubic crystal.[22,32] (2) The covalent nature of Pt-I bonds in $[PtI_6]^{2-}$ octahedra, which may inhibit hydrated phase formation.[25] (3) Negative formation energies (E_{f_1} and E_{f_2}) suggesting thermodynamic structural stability and ease of synthesis ($E_{f_1} = \frac{E_{Cs_2PtI_6} - 2E_{Cs} - E_{Pt} - 6E_I}{36}$ and $E_{f_2} = E_{Cs_2PtI_6} - 2E_{CsI} - E_{PtI_4}$). The negative E_{f2} value implies that experimental synthesis of the material is feasible, whereas the negative E_{f1} value confirms its thermodynamic structural stability.[31,41] (4) A stable oxidation state of Pt^{4+}. (5) A phonon dispersion that is well-converged and shows positive frequencies across the entire Brillouin zone demonstrates the material's dynamic stability.[30]

Theoretical studies have predicted that when Cs_2PtI_6 undergoes substitution doping with a smaller-radius halogen such as Cl and Br, the formation energy decreases, thus further enhancing structural stability in order of Cs_2PtCl_6 ($\Delta H = -11.25$) > Cs_2PtBr_6 ($\Delta H = -10.11$) > Cs_2PtI_6 ($\Delta H = -7.44$).[31] This prediction aligns with experimental observations by Muhammed et al., who found that thermal stability increases as the halide changes from I to Cl.[19] Thermogravimetric analysis performed under nitrogen revealed that Cs_2PtCl_6 maintained 95% of its weight up to about 600°C, while Cs_2PtBr_6 retained 95% of its weight at 458°C. Both of Cs_2PtBr_6 and Cs_2PtCl_6 show higher thermal stability than Cs_2PtI_6 (~ 350–364°C) (as shown in Figure 2C). The greater

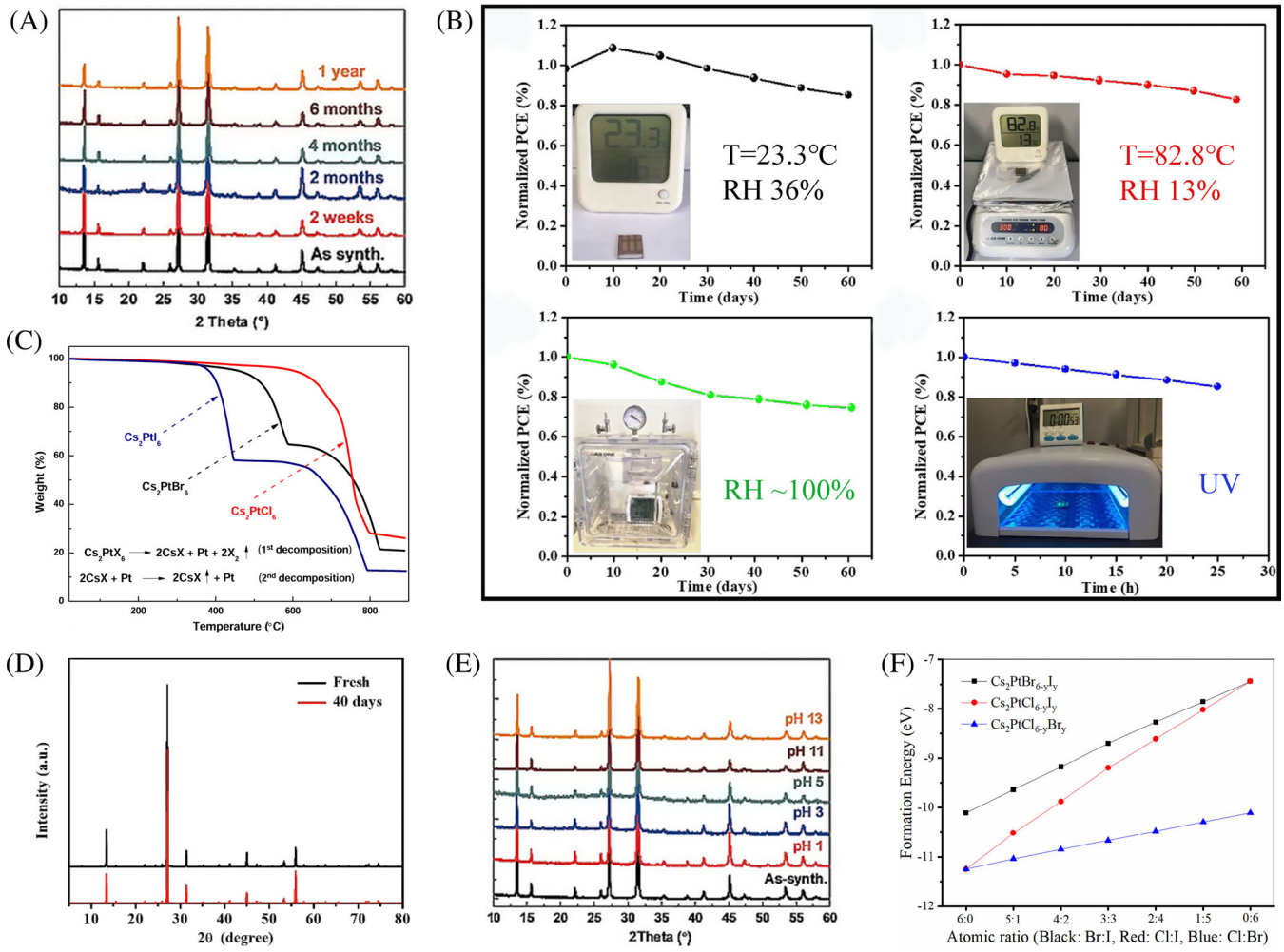

FIGURE 2 Stability. (A) x-ray diffraction patterns of Cs_2PtI_6 showing extraordinary stability under ambient conditions over 1 year. (B) Longtime stability of the Cs_2PtI_6 solar cell under ambient conditions without encapsulation, at high temperature, at high humidity, or under UV radiation. (C) Thermogravimetric analysis of Cs_2PtI_6, Cs_2PtBr_6 and Cs_2PtCl_6 (under nitrogen), respectively. Reproduced with permission: Copyright 2022, John Wiley and Sons.[19] (D) x-Ray crystallography (XRD) diffraction patterns of Cs_2PtI_6 powder before and after 40 days in water. The (b) and (D) are reproduced with permission: Copyright 2020, American Chemical Society.[22] (E) XRD patterns of Cs_2PtI_6 after exposing them to aqueous solutions of various pH values for 4 h. (A) and (e) are reproduced with permission: Copyright 2020, John Wiley and Sons.[20] (F) The formation energy of Cs_2PtX_6 (X = Cl, Br, and I). The abscissa represents the ratio of two halogens in the compounds. Reproduced with permission: 2022, John Wiley and Sons.[31]

thermal stability observed in Cs_2PtCl_6 is attributed to the stronger Pt—Cl bonds in comparison to Pt—Br and Pt—I bonding. Reported bond energies for Pt—Cl and Pt—Br in K_2PtCl_6 and K_2PtBr_6, respectively, were 1551 and 1545 kJ/mol.[46] Cs_2PtBr_6 and Cs_2PtCl_6, like Cs_2PtI_6, also exhibit exceptional acidic and basic aqueous stability across pH range from 1 to 13, and they demonstrate good performance in water splitting.[19,23]

Experimental studies on A-site substitution are scarce, with simulations indicating its significant influence on stability (e.g., $Cs_2PtI_6 > Rb_2PtI_6 > K_2PtI_6 > Tl_2PtI_6$), primarily through structural modifications.[41] Experimental evidence reveals that substituting Cs^+ with ions of smaller ionic radii, such as Rb^+ and K^+, reduces the thermal stability of the vacancy-ordered perovskite A_2PtI_6. Cs_2PtI_6 can withstand temperatures ranging from 350 to 364°C, however, Rb_2PtI_6 and K_2PtI_6 are stable up to 328°C and 308°C, respectively. Additionally, while Cs_2PtI_6 maintains stability in solutions with pH levels between 7 and 11, Rb_2PtI_6 and K_2PtI_6 dissolve or decompose immediately under similar conditions. These findings highlight the critical role of A-site in determining their stability and performance.[21] More information about the stability parameters of A_2PtX_6 Pt halide double perovskites is summarized in Table 2.

2.4 | Electronic structure and properties

As an efficient photovoltaic material, Cs_2PtI_6 demonstrates advanced electronic properties, including a high

TABLE 2 Stability parameters of A_2PtX_6 Pt halide double perovskites.

Compound	Thermal stability	Aqueous (pH) stability	PCE stability	Long term stability	References
Cs_2PtI_6	2% weight loss up to 300°C	–	–	2 months (60 days)	18
Cs_2PtI_6	Stable up to around 250°C	Over 24 h in aqueous from pH 1 and pH 13	Over 12 h 0.384 V versus Ag/AgCl (the equivalent of 1.23 V vs. RHE)	1 year in air	20
Cs_2PtI_6	Stable up to around 364°C	Stable in dichloromethane (DCM) for 24 h; stable in solution of pH 7–11	BiVO4/Cs2PtI6; 0.5 V versus Ag/AgCl (equivalent to 1.23 V vs. RHE) in pH 9 electrolyte.; stable in 300 s of run. decrease 50% in 1 h and sustained for nearly 2 h	–	21
Cs_2PtI_6	No significant weight loss at 300°C	No signs of decomposition immersing in water	–	Ambient conditions at 23°C with an RH of 36%,80% PCE 60 days; 80°C 80% PCE 60 days; high humidity (∼100%) 80% PCE 60 days; ultraviolet radiation (36 W), 80% PCE 24 h	22
Cs_2PtCl_6	Retained 95% weight until ∼600°C	4 h in aqueous from pH 1 to pH 13	2 h 0.384 V versus Ag/AgCl (1.23 V vs. RHE)	–	19
Cs_2PtBr_6	Retained 95% weight until ∼458°C	4 h in aqueous from pH 1 to pH 13	2 h 0.384 V versus Ag/AgCl (1.23 V vs. RHE)	–	19
Cs_2PtBr_6 NC	Stable 100°C for 10 h	Stable in pH 8	Relatively stable in 30 on/off cycles in 600 s (RSD = 2.6%)	LED light (10 mW cm^{-2}, 365 nm for 10 h); Moisture (RH ∼ 55%) in dark 60 days	23
Rb_2PtI_6	Stable up to around 328°C	Stable in dichloromethane (DCM) for 24 h; dissolved/decomposed immediately in solution of pH 7-11	–	2 weeks	21
K_2PtI_6	Stable up to around 308°C	Stable in dichloromethane (DCM) for 24 h; dissolved/decomposed immediately in solution of pH 7–11	Oxidizes significantly at 0.6 V (vs. Ag/AgCl)	2 weeks	21

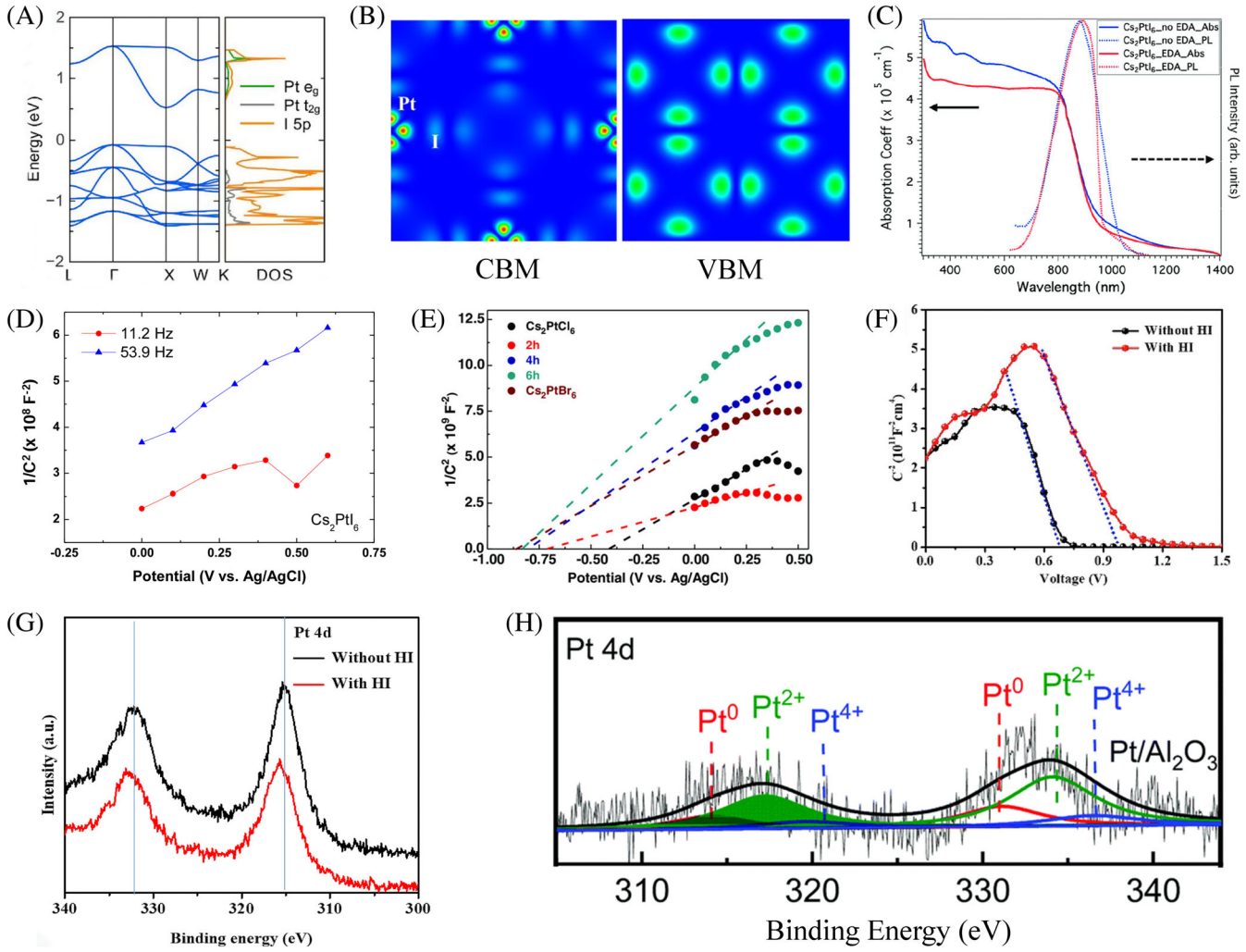

FIGURE 3 Photoelectronic properties. (A) The calculated electronic structures of Cs_2PtI_6. (B) CBM and VBM of Cs_2PtI_6. The (A) and (B) are reproduced with permission: Copyright 2020, American Chemical Society.[22] (C) UV–Vis absorption coefficient and PL emission spectra of Cs_2PtI_6. Reproduced with permission: Copyright 2020, John Wiley and Sons.[17] (D) Mott–Schottky plots for Cs_2PtI_6 in pH 9 solution. Reproduced with permission: Copyright 2021, American Chemical Society.[21] (E) Mott–Schottky plot of the Cs_2PtCl_6, Cs_2PtBr_6, and core–shell materials at various conversion times. Reproduced with permission: 2022, John Wiley and Sons.[19] (F) Mott–Schottky curve of Cs_2PtI_6. (G) XPS Pt 4d spectrums of the Cs_2PtI_6 (w/wo HI). The (F) and (G) are reproduced with permission: Copyright 2020, American Chemical Society.[22] (H) XPS spectra showing the standard banding energy of Pt^0, Pt^{2+}, and Pt^{4+}, respectively. Reproduced with permission: Copyright 2021, The Royal Society of Chemistry.[50]

absorption coefficient exceeding 10^5 cm^{-1} across a wide wavelength range (as shown in Figure 3C), a suitable bandgap of approximately 1.4 eV, aligning well with the Shockley–Queisser limit where bandgap for optimal efficiency of photovoltaic materials falls within the range of 1.3–1.4 eV,[47] and a carrier lifetime exceeding 2 μs.[17] In Cs_2PtX_6 compounds, the outermost p-orbitals of the halogen atoms typically contribute to the valence band maximum (VBM), while the conduction band minimum (CBM) is predominantly composed of the d-orbitals of Pt combined with the outermost p-orbitals of the halogen atoms. In Cs_2PtI_6, as shown in Figure 3A,B, the VBM mainly comprises the 5p-orbitals of iodine, while the CBM primarily results from the interaction between Pt e_g-orbitals with I 5p-orbitals.[22]

Doping with halogen atoms has been reported to alter the band structure type of Cs_2PtX_6, though it does not fundamentally change its main characteristics.[31] Theoretical studies suggest that doping Cs_2PtCl_6 with bromide or iodide to generate $Cs_2Pt_yCl_{6-y}$ and $Cs_2PtI_yCl_{6-y}$ can shift the band structure type from direct to indirect.[31] Moreover, increasing the content of bromide and iodide leads to a greater contribution from the heavier halogens with higher energy orbitals (Br-4p and I-5p compared to Cl-3p), shifting the projected density of states (PDOS) towards higher energies and closer to the Fermi energy,

resulting in a reduced bandgap. Thus, the bandgap follows the trend $Cs_2PtI_6 < Cs_2PtBr_6 < Cs_2PtCl_6$, consistent with experimental observations. Hamdan et al. reported band gaps for Cs_2PtI_6, Cs_2PtBr_6, and Cs_2PtCl_6 are 1.3, 1.88, and 2.16 eV respectively.[19–21] The variation in bandgap can be attributed to differences in electronegativity (Cl > Br > I) and atomic radius (I > Br > Cl). The substantial difference in Pt-Cl bond length relative to Pt-Br and Pt-I results in a larger bandgap for Cl-doped perovskites compared to those doped with other halogens.[31]

Although the A-site ions (e.g., Cs^+, Rb^+, and K^+) do not directly participate in forming energy bands at the CBM and VBM, as in lead halide perovskite, instead they indirectly influence the band structure through structural distortion.[48] For example, substituting Cs^+ ions into ions of smaller ionic radii (Rb^+ and K^+) was experimentally observed to increase the band gap. The bandgaps for Cs_2PtI_6, Rb_2PtI_6, and K_2PtI_6 were reported as 1.3, 1.33, and 1.36 eV, respectively.[21] This rise in the bandgap was ascribed to the octahedron distortion, which influences the interaction between Pt and I in the crystal lattice.

Additionally, there is controversy regarding whether Cs_2PtX_6 semiconductors exhibit n-type or p-type characteristics. The synthesized Cs_2PtI_6, Cs_2PtBr_6, and Cs_2PtCl_6 by the Chandiran group, employing chloroplatinic acid hexahydrate (Pt in 4+ oxidation state) with Pt content exceeding 37%, consistently exhibiting a positive slope in the Mott–Schottky plot (Figure 3D,E).[19] This analytical method, measuring the impedance response at a frequency of 100 Hz within a voltage range of 0–0.5 V (vs. Ag/AgCl), reliably indicated the n-type conductivity of Cs_2PtX_6 (X = Cl, Br, and I). Moreover, the incorporation of a Cs_2PtI_6 additive into $Cs_{0.05}(FA_{0.95}MA_{0.05})_{0.95}Pb(I_{0.95}Br_{0.05})_3$-based perovskite solar cell has been demonstrated to elevate the surface potential.[29] A notable surface potential increase of 60–70 mV compared to control films was reported. This increase in surface potential was ascribed to the n-type conductivity of the Cs_2PtI_6 additive, which caused an upward shift in the Fermi energy level and thereby enhances the n-type conductivity of the absorber. Such findings corroborate similar observations reported by Chen et al. of Cs_2PtI_6-based NO gas detectors, where the N-Pt bond demonstrates a transfer of 0.22 negative charge from Pt to N, attributing to n-type doping of Cs_2PtI_6.[18] DFT calculations also indicate the electron transport in Cs_2PtI_6 is better than hole transport (effective masses $m_e^* = 0.48\,m_0$, $m_h^* = 1.57\,m_0$;[49] $\mu_h = 62.6\,cm^2.V^{-1}.s^{-1}$),[17] in line with its n-type characteristics. However, Yang et al. exhibit a contrasting p-type behavior for Cs_2PtI_6, substantiated by the negative slope observed in the Mott–Schottky plot (Figure 3F).[22] Remarkably, the Cs_2PtI_6 here is synthesized from PtI_2, suggesting the potential to modulate charge carrier behavior through nuanced precursor selections or material synthesis methodologies. Comparison of XPS data for Pt 4d peak with standard binding energy (Figure 3H),[50] suggests that here Cs_2PtI_6 comprises of a certain proportion of Pt^0 (Figure 3G), suggesting oxidation transformation of $2Pt^{2+} \rightarrow Pt^{4+} + Pt^0$ in the presence of HI and DMSO. Our recent investigations have shown formation of 2D layered perovskite phase, $CsPtI_3$(DMSO), with PtI_2 precursor in DMSO solvent. The 2D phase transforms to mixed phase of Cs_2PtI_6 and Pt at temperature of 181.5°C, which decomposes to CsI and Pt at 382.5°C.[51] Synthesis of mixed Cs_2PtI_6 and Pt has also been reported from PtI_2 precursor with different annealing conditions and solvent engineering.[22,51] Excess Pt sites in Cs_2PtI_6 may serve as electron traps, impeding electron–hole recombination through facilitated charge transfer and electron accumulation.[50,52] Moreover, the effective charge transfer from Cs_2PtI_6 to Pt holds promise for various applications in photocatalysis, particularly in processes such as water splitting where Pt can serve as a catalytic site for reaction $2H_{ad} \rightarrow H_2$.[50,52–54] Peng et al. also stated that the Cs_2PtBr_6 exhibits the p-type property since the enhanced photocurrent intensity with the increase of cathodic potential.[23] In conclusion, the Cs_2PtX_6 double perovskite can exhibit both n- and p-type conductivity depending upon processing and chemical potential change from Pt-poor to Pt-rich conditions. More studies about the photoelectronic properties of A_2PtX_6 Pt halide double perovskites are summarized in Table 3.

2.5 | Other transition metal vacancy ordered double perovskites

Vacancy-ordered halide double perovskites exhibit broad-spectrum visible light absorption and stability, even when exposed to acidic and basic aqueous solutions, typically used in photoelectrochemical (PEC) studies. In addition to the extensively studied platinum-based vacancy-ordered double perovskites, recent research has also increasingly focused on rhenium (Re),[55] osmium (Os),[56,57] palladium (Pd),[58–60] ruthenium (Ru),[61] and zirconium (Zr),[62–66] as shown in Figure 4 and summarized in Table 4. These materials also show significant potential for applications like PEC or near-infrared light-emitting diodes (NIR-LEDs).

2.5.1 | Pd-based vacancy ordered double perovskites

Sakai et al. first report the solution processable Cs_2PdBr_6.[60] It also shows a space group $Fm\bar{3}m$ (no. 225) as Cs_2PtX_6. DFT-HSE analysis revealed an indirect fundamental bandgap of 1.56 eV ($\Gamma \rightarrow X$), however, the lowest

TABLE 3 Photoelectronic properties of A_2PtX_6 Pt halide double perovskites.

Compound	Bandgap (eV)	Type	CBM (eV)	VBM (eV)	References
Cs_2PtI_6	1.37 (indirect)	–	−4.3	−5.67	22
Cs_2PtI_6	1.26	n-type			18
Cs_2PtI_6	1.25	n-type	–	–	20
Cs_2PtI_6	1.3	n-type	∼ 0.5 (vs. NHE)	∼ 1 (vs. NHE)	21
Cs_2PtI_6	1.36–1.4 (indirect)				17
Cs_2PtI_6	1.4	–	−0.12 (vs. NHE)	1.3 (vs. NHE)	26
Cs_2PtI_6	1.35	P type	–	–	25
Cs_2PtI_6	-	P type			30
Cs_2PtI_6	1.39 (indirect)	–	–	–	32
$Cs_2PtI4Br_2$	1.6	–	−0.09 (vs. NHE)	1.5 (vs. NHE)	26
$Cs_2PtI_2Br_4$	1.7	–	−0.02 (vs. NHE)	1.7 (vs. NHE)	26
Cs_2PtBr_6	2.6	–	−0.03 (vs. NHE)	2.3 (vs. NHE)	26
Cs_2PtBr_6	1.32	p-type	−3.67	−4.99	23
Cs_2PtBr_6	1.88 (indirect)	n-type	−3.84 (vs. Ag/AgCl)	−5.72 (vs. Ag/AgCl)	19
Cs_2PtBr_6	2.33 (direct)		−4.4	−6.73	32
Cs_2PtCl_6	2.16 (direct)	n-type	−4.28 (vs. Ag/AgCl)	−6.44 (vs. Ag/AgCl)	19
Rb_2PtI_6	1.33	–	–	–	21
K_2PtI_6	1.36	–	–	–	21
In_2PtCl_6	2.290 (indirect)	–	–	–	28
In_2PtBr_6	1.926 (direct)	–	–	–	28
In_2PtI_6	1.301 (indirect)	–	–	–	28
Tl_2PtCl_6	3.238 (indirect)	–	–	–	28
Tl_2PtBr_6	2.452 (indirect)	–	–	–	28
Tl_2PtBr_6	1.295 (indirect)	–	–	–	28

Abbreviations: CBM, conduction band minimum; VBM, valence band maximum.

direct bandgap (1.59 eV at X) is only 30 meV larger than the indirect bandgap, as shown in Figure 4A. The VBM (−6.47 eV) is made of Br-p orbital and CBM (−4.86 eV) is made of Pd-4d orbital and Br-4p orbital, while nonbonding character of the electrons localized on Cs. Cs_2PbBr_6 behaves as n-type semiconductor with smaller effective mass of electrons (0.53 m_e) than light holes (0.85 m_e) and heavy holes (19.9 m_e), and Fermi level (−4.95 eV) is close to the CBM. The optical band gap of 1.6 eV, derived from UV–Vis absorption and steady-state photoluminescence (PL) measurements, is consistent with the values obtained from DFT-HSE calculations, with a carrier lifetime of 1.85 and 79 ns for single crystal and thin film, respectively, estimated using a mono-exponential function fit for TRPL decay data. Cs_2PdBr_6 is also proved as a water stable compound without obvious phase change and chemical decomposition through water immersion test. Zhou et al. also synthesized ligand-free Cs_2PdBr_6 and Cs_2PdI_6 cubic perovskite nanocrystals.[58] The Cs_2PdBr_6 nanocrystals exhibit a higher optical bandgap (1.69 eV) compared to their microcrystalline powder form (1.49 eV), due to quantum confinement effect. Cs_2PdBr_6 nanocrystals exhibit excellent stability when subjected to long-term light exposure (1 sun for over 1000 h), moisture (70% humidity for 2 months), and high temperatures (120°C for 600 h). Through an anion exchange reaction, Cs_2PdBr_6 nanocrystals can be converted to Cs_2PdI_6 nanocrystals, which have a smaller bandgap (1.41 eV). Ultrafast transient absorption (TA) spectroscopy measurements revealed rapid trapping processes due to surface defects, resulting in relatively short PL decay lifetime

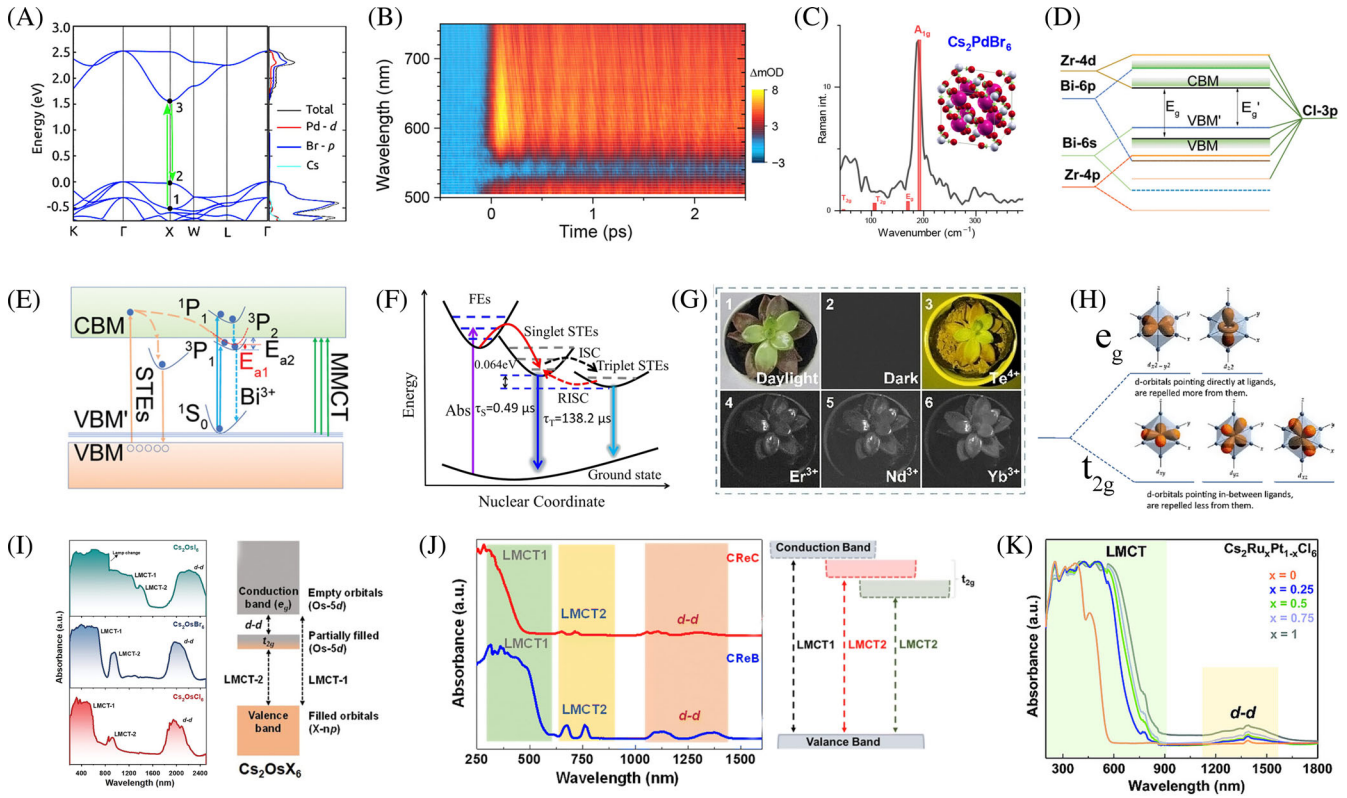

FIGURE 4 Other transition metal-based vacancy ordered double perovskite. (A) Electronic band structure of Cs_2PdBr_6. Reproduced with permission: Copyright 2017, American Chemical Society.[60] (B) Contour plot of the transient absorption for a Cs_2PdBr_6 thin film showing significant oscillations, indicative of coherent phonon dynamics. (C) Raman activity of Cs_2PdBr_6. The (B) and (C) are reproduced with permission: Copyright 2023, American Chemical Society.[59] (D) Schematic energy diagram of Cs_2ZrCl_6 and Cs_2ZrCl_6:Bi^{3+}. (E) Energy level diagram for the fluorescence mechanism of Cs_2ZrCl_6 and Cs_2ZrCl_6: Bi^{3+}. The (D) and (E) are reproduced with permission: Copyright 2020, John Wiley and Sons.[66] (F) Schematic diagram of PL mechanism of Cs_2ZrCl_6 NCs. Reproduced with permission: Copyright 2020, John Wiley and Sons.[65] (G) Night-version application of Cs_2ZrCl_6: Te^{4+}/Ln^{3+} phosphors. Reproduced with permission: Copyright 2022, John Wiley and Sons.[63] (H) The wavefunctions of t_{2g} and e_g states. In an octahedra crystal field, the five d states orbital will split into a triplet t_{2g} (d_{xy}, d_{xz}, and d_{yz}) with lower energy and double e_g ($\boldsymbol{d_{x^2-y^2}}$ and $\boldsymbol{d_{z^2}}$) level with higher energy. The crystal field splitting is basically due to electrostatic attractive and repulsive interactions from negative charge at each vertex of an octahedron. Reproduced with permission: Copyright 2018, American Physical Society.[68] (I) Absorption spectra reveal transitions associated with ligand-to-metal charge transfer (LMCT) and d-d transitions within Os-5d orbitals. Reproduced with permission: Copyright 2022, John Wiley and Sons.[57] (J) Absorption spectra of Cs_2ReCl_6 and Cs_2ReBr_6. Reproduced with permission: Copyright 2023, The Royal Society of Chemistry.[55] (K) Absorption spectra of $Cs_2Ru_xPt_{1-x}Cl_6$. Reproduced with permission: Copyright 2024, John Wiley and Sons.[61]

($\tau_{ave} = 1.5$ ns for microcrystal and $\tau_{ave} = 0.9$ ns for nanocrystal) and low photoluminescence quantum yield (PLQY) of 0.3%.[58] The observation is in line with the combined spectroscopic and electrical studies by Scholz et al. on Cs_2PdBr_6, which conclude a trap-mediated electron–hole recombination mechanism.[59] The defect energy was found to be $E_d = 1.23$ eV, which is 0.33 eV below the indirect band gap. These deep defects, V_{Br} and V_{Pd}, act as nonradiative recombination sites and decrease the device V_{OC}. Moreover, a strong electron–phonon coupling is indicated by pronounced coherent oscillations, as shown in Figure 4B. DFT analysis identifies the A_{1g} Raman-active optical phonon mode (Figure 4C) as the source of substantial kinetic oscillations. This mode involves the symmetric stretching of Pd—Br bonds within the octahedral cages, driven by the coordinated movement of the bromide ions. The electron–phonon coupling can also result in non-radiative recombination in addition to deep defect states. Consequently, despite Cs_2PdBr_6 exhibiting a wide absorption spectrum and good stability, it falls short as an ideal photovoltaic absorber due to its indirect band gap, deep trap states, and pronounced electron–phonon coupling.

2.5.2 | Zr-based vacancy ordered double perovskites

Cs_2ZrCl_6 was early explored about its luminescence by Bryan et al. for making efficient luminophores.[64] The emission of Cs_2ZrCl_6 requires high-energy wavelength

TABLE 4 Other transition metal-based vacancy-ordered double perovskites.

Compounds	Type	Bandgap (eV)	CBM (eV)	VBM (eV)	Stability	References
Cs_2ZrCl_6	–	3.57	–	–	–	60
10% Bi^{3+}-doped Cs_2ZrCl_6	–	3.36	–	–	373 K, 423 K for 30 min; 2 h immerge in water; 24 h ambient under 350 nm UV	66
Cs_2ZrCl_6 NC	–	4.86	–	–	Thermal stability up to 650°C and long-term air stability for over 6 months	65
$Cs_2ZrBr_{1.5}Cl_{4.5}$ NC	–	4.76	–	–	–	65
Cs_2ZrCl_6	–	3.45	–	–	–	62
1%Te:Cs_2ZrCl_6	–	3.22	–	–	Structure stability 2 month in air	62
50%Te:Cs_2ZrCl_6	–	2.92	–	–	–	62
Cs_2PdBr_6	n-type	1.6	−4.86	−6.47	10 min water immersion test	60
Cs_2PdBr_6 nanocrystal	–	1.69	−4.94	−6.63	1000 h 1sun illumination in air; 2 months in 70% humidity (25°C); 600 h under 120°C	58
Cs_2PdBr_6 microcrystal	–	1.49	−5.01	−6.5	–	58
Cs_2PdI_6 nanocrystal	–	1.41	–	–	–	58
Cs_2OsI_6	n-type	0.94	−0.11 (Ag/AgCl at pH 11)	0.83 (Ag/AgCl at pH 11)	400°C (TGA); 10 months in ambient; 24 h between pH 1 and pH 11	57
Cs_2OsBr_6	n-type	1.7	−0.14 (Ag/AgCl at pH 11)	1.56 (Ag/AgCl at pH 11)	500°C (TGA); 10 months in ambient; 24 h between pH 1 and pH 11	57
Cs_2OsCl_6	n-type	1.99	−0.2 (Ag/AgCl at pH 11)	1.79 (Ag/AgCl at pH 11)	650°C (TGA); 10 months in ambient; 24 h between pH 1 and pH 11	57
Cs_2ReBr_6	n-type	2.2	−4.5	−6.7	∼600°C(TGA); 24 h between pH 1 and pH 11	55
Cs_2ReCl_6	n-type	2.7	−4.44	−7.14	∼600°C(TGA); 24 h between pH 1 and pH 11	55
Cs_2RuBr_6	n-type	1.2	−0.05 (Ag/AgCl)	1.15 (Ag/AgCl)	∼448°C (TGA 95% weight)	61
$Cs_2Ru_{0.75}Pt_{0.25}Br_6$	n-type	1.22	–	–	–	61
$Cs_2Ru_{0.5}Pt_{0.5}Br_6$	n-type	1.24	–	–	∼530°C (TGA 95% weight)	61
$Cs_2Ru_{0.25}Pt_{0.75}Br_6$	n-type	1.27	–	–	–	61
Cs_2PtBr_6	n-type	1.89	−0.82 (Ag/AgCl)-	1.07 (Ag/AgCl)-	∼536°C (TGA 95% weight)	61
Cs_2RuCl_6	n-type	1.65	−0.1 (Ag/AgCl)	1.55 (Ag/AgCl)	∼518°C (TGA 95% weight)	61
$Cs_2Ru_{0.75}Pt_{0.25}Cl_6$	n-type	1.74	–	–	–	61

(Continues)

TABLE 4 (Continued)

Compounds	Type	Bandgap (eV)	CBM (eV)	VBM (eV)	Stability	References
$Cs_2Ru_{0.5}Pt_{0.5}Cl_6$	n-type	1.8	–	–	~570°C (TGA 95% weight)	61
$Cs_2Ru_{0.25}Pt_{0.75}Cl_6$	n-type	1.9	–	–	–	61
Cs_2PtCl_6	n-type	2.23	−0.41 (Ag/AgCl)-	1.82 (Ag/AgCl)-	680°C (TGA 95% weight)	61

Abbreviations: CBM, conduction band minimum; VBM, valence band maximum.

excitation. To expand the application, efforts are made for modifying the optoelectronic properties of Cs_2ZrCl_6 through doping technique. Xiong et al.[66] and Liu et al.[65] successfully heterovalently doped Cs_2ZrCl_6 with activator Bi^{3+} (B site doping) for controllable bandgap engineering and ionoluminescence. Pristine Cs_2ZrCl_6 crystallizes in a cubic structure with space group $Fm\bar{3}m$ and a lattice constant of 10.438 Å.[66] Figure 4D illustrates that the VBM is primarily derived from Cl 3p orbitals, and the CBM is predominantly formed by Zr 4d and Cl 3p orbitals. In Bi^{3+}-doped Cs_2ZrCl_6, the CBM still consists of Zr 4d and Cl 3p orbitals, but the VBM is influenced by Bi 6s orbitals. Increasing the Bi^{3+} atomic concentration from 0 to 0.1 reduces the bandgap from 3.57 to 3.36 eV. An increase in Bi^{3+} atomic concentration to 0.3 causes the bandgap to slightly increase to 3.39 eV. As depicted in Figure 4E, the undoped Cs_2ZrCl_6 displays a blue self-trap exciton (STE) emission at approximately 454 nm with PLQE of 31% and full width at half maximum (FWHM) of 103 nm. Bi^{3+} doping modifies the electron dynamics, leading to a narrower ionoluminescence peak at about 456 nm (FWHM = 63 nm) and an enhanced PLQY of around 50%. The Bi^{3+} doped Cs_2ZrCl_6 shows thermal stability over 373 K and 423 K for 30 min, however decomposition triggered by water and moisture. Liu et al. also synthesized $Cs_2ZrBr_xCl_{6-x}$ (X-site halogen anion substitution) nanocrystals with adjustable PL emission.[65] Cs_2ZrCl_6 NCs show a bandgap of 4.86 eV, with a broadband PL emission peaked at 446 nm with a FWHM of 138 nm and a large Stokes shift of 201 nm. The significant Stoke shift and broad emission spectrum imply that the PL could be attributed to STEs. Due to the flexible lattice structure of metal halides, photoelectrons interact with lattice vibrations at the excited-state energy level. This interaction causes transient lattice distortions, alterations in nuclear coordinates, and the formation of localized STEs.[67] The emission mechanism is illustrated in Figure 4F. A fast decay component is also assigned to the intersystem crossing (ISC) from singlet STEs to triplet states, with long-lived triplet excited state (138.2 μs) and PLQY of 60.37%.[65] The Cs_2ZrCl_6 nanocrystals also show excellent thermal stability up to 650°C and remain stable in air for more than 6 months. By substituting halogens in $Cs_2ZrBr_xCl_6$-x NCs (where $0 < x < 1.5$), the optical characteristics of these nanocrystals were modified. Increasing the bromine content reduces the optical band gap from 4.86 eV in Cs_2ZrCl_6 to 4.76 eV in $Cs_2ZrBr_{1.5}Cl_{4.5}$, shifts the emission color from blue to green, and shortens the triplet emission lifetime due to the heavy-atom effect. Chang et al.[62] and Sun et al.[63] reported their effort on B-site doping Cs_2ZrCl_6 with Te^{4+} and Ln^{3+} (Er^{3+}, Nd^{3+}, and Yb^{3+}). With Te^{4+} doping, an efficient singlet-triplet energy transfer emission was also observed, and a green

yellow (575 nm) triplet STE emission of Te^{4+} ion with high PLQY of 49% was obtained.[62] At reduced temperature, the relative intensity of triplet STE emission rises because the weakened electron–phonon coupling facilitates the ISC process. The band gaps of pure Cs_2ZrCl_6, 1% Te:Cs_2ZrCl_6, and 50% Te:Cs_2ZrCl_6 are 3.45, 3.22, and 2.92 eV, respectively. An increase in the Te^{4+} content within Cs_2ZrCl_6 results in a reduced bandgap. This change is due to the higher energy level of the lowest Te 5p orbital and the lower energy level of the highest Te 5s orbital. Rb^+ A-site alloying was proved to increase stability. Lanthanide (Ln^{3+}) ions like Yb^{3+}, Nd^{3+}, and Er^{3+} are capable of emitting near-infrared photons. However, their emission is constrained by low absorption coefficients arising from the parity-forbidden transitions in their $4f^N$ electron configurations.[63] With co-doping of Te^{4+}/Ln^{3+} in Cs_2ZrCl_6, the intense NIR luminescence in various wavelength originating from the intra-4fN transition of Yb^{3+}, Nd^{3+}, and Er^{3+} ions were achieved through sensitization by Te^{4+}.[63] The Te^{4+} singly-doped and Te^{4+}/Ln^{3+} co-doped Cs_2ZrCl_6 MCs also shows good structural thermal stability (565°C) and long-term stability (3 month in ambient). LED devices was fabricated by encapsulating Cs_2ZrCl_6: Te^{4+}/Ln^{3+} phosphors onto a commercial 392 nm near-ultraviolet light (NUV)- LED chips, reveal the great potentials in diverse areas such as NIR spectroscopy, food testing, bioimaging, and night vision, as shown in Figure 4G.[61,62]

2.5.3 | Os-based vacancy ordered double perovskites

Shanmugam et al. investigated the osmium-based vacancy-ordered double perovskites Cs_2OsX_6 (where X = Cl^-, Br^-, and I^-), revealing their distinctive optical and photoelectrochemical characteristics, particularly the d-orbital splitting and d-d transition.[57] Cs_2OsX_6 also adopts a zero-dimensional (0D) structure with an $Fm\bar{3}m$ space group. In these compounds, osmium is in the +4-oxidation state, exhibiting a $5d^4$ electronic configuration. Compared to 3d elements, the 5d elements have spatially more extended d orbitals, resulting in strong hybridization with neighboring ligand atoms and leading to significant crystal field splitting.[68] As illustrated in Figure 4H, the five d orbitals split into a triplet t_{2g} level and a double e_g level under octahedra crystal field effect. For 5d elements, the crystal field splitting is significantly greater than the spin pairing energy, causing the d orbital electrons to first pair up and fill the lower energy t_{2g} orbitals, while the higher energy e_g orbitals remain unoccupied in the d^1-d^6 configurations.[56] In the case of Cs_2OsX_6, the e_g and t_{2g} levels split further under O_h symmetry and additional symmetry lowering. As shown in Figure 4I, the VBM is made of the filled p-orbitals of halide (X-np), while the CBM is made of empty Os-5d e_g orbital, band positions are summarized in Table 4. The partially filled Os-5d t_{2g} orbital (↑↓, ↑, and ↑) sits between as mid-gap state. The electronic configuration is reflected in the absorption spectroscopy shown in Figure 4I. The pronounced absorption in the 300–600 nm range is associated with ligand-to-metal charge transfer (LMCT-1) from the X-np VBM to the Os-5d e_g orbital at CBM. Meanwhile, the infrared peak near 920 nm is attributed to LMCT-2, involving charge transfer between the VBM and the Os-5d t_{2g} mid-gap state.[57] The broader infrared peak observed in range of 1800–2500 nm is attributed to d-d transitions involving the partially filled Os-5d t_{2g} orbital and empty Os-5d e_g orbital. Substituting I into Br and Cl increases the lattice parameter, red-shift the LMCT-1 absorption, and decreases the bandgap by moving up the energy level of VBM. Electrochemical impedance (EIS) measurements revealed the n-type characteristics with positive slope in Mott–Schottky (M–S) plot. Cs_2OsX_6 also exhibits excellent stability under ambient conditions (10 months), varying pH levels in aqueous solution (24 h between pH 1 and pH 11), and high temperatures (400°C for Cs_2OsI_6, 500°C for Cs_2OsBr_6, and 650°C for Cs_2OsCl_6).

2.5.4 | Re-based vacancy ordered double perovskites

Chandra et al. reported two n-type rhenium-based vacancy-ordered double perovskites, Cs_2ReCl_6 and Cs_2ReBr_6, also in $Fm\bar{3}m$ space group.[55] In these materials, tetravalent rhenium (Re^{4+}) possesses a $5d^3$ valence state, also belonging to the d^1-d^6 configuration. Consequently, there is also a d-orbital splitting with the t_{2g} orbitals are partially filled (↑, ↑, and ↑), while the e_g orbitals remain unoccupied, similar to Cs_2OsX_6. This configuration permits optical transitions from the valence orbitals of the ligand (halide p-orbitals) to either the partially filled t_{2g} orbitals or the vacant e_g orbitals. As a results, the absorption spectrum, shown in Figure 4J, displays two ligand-to-metal charge transitions processes, LMCT1 and LMCT2. LMCT1, observed as absorption at 500 nm for Cs_2ReCl_6 and 600 nm for Cs_2ReBr_6, corresponding to transitions between halide p-orbitals (VBM) and the vacant metal e_g states (CBM). LMCT2 is characterized by two red absorption peaks resulting from transitions between halide p-orbitals (VBM) and the non-degenerate t_{2g} orbitals (mid-gap states), where the t_{2g} orbital may exist in two distinct energy levels. Additionally, d-d transitions between the partially filled t_{2g} and

empty e_g levels lead to transition in the IR region. This behavior contrasts with Cs_2PtX_6, where platinum in the +4-oxidation state has a $5d^6$ electronic configuration with fully occupied t_{2g} orbitals and empty e_g orbitals. This configuration accounts for the lack of LMCT2 transitions in the absorption spectrum of Cs_2PtX_6.[17,61] Besides excellent visible and NIR absorption, Cs_2ReX_6 vacancy-ordered double perovskite also exhibits high stability under ambient conditions, in acidic to basic aqueous environments (pH 1–pH 11), and at temperatures up to around 600°C. Attributing to the demonstrated stability in these harsh environments, suitable band positions and conductivity, this material is a potential photoanode for solar water oxidation in alkaline media. It was confirmed with clear light dependent current in the photoelectrochemical system.[55]

2.5.5 | Ru-based vacancy ordered double perovskites

Halpati et al. successfully synthesized vacancy-ordered halide double perovskites Cs_2RuX_6 and $Cs_2Ru_mPt_{1-m}X_6$ ($X = Cl^-$ and Br^-) and demonstrated their application in solar water oxidation.[61] The Cs_2RuCl_6 and Cs_2RuBr_6 crystallize in same crystal structure as Cs_2PtX_6, showing a n-type characteristic. The optical absorption spectrum also uncovers the LMCT from Cl-3p or Br-4p orbitals to Ru-4d orbitals, along with the d-d transitions between the e_g and t_{2g} states of the metal d orbitals. This is evident from the strong absorption at short wavelengths and low-intensity absorption in the infrared range (1200–1700 nm), as illustrated in Figure 4K. Cs_2PtX_6 shows extraordinary basic pH stability (to pH 14), better than Cs_2OsX_6 and Cs_2ReX_6, and better photovoltage, thus was incorporated in the Ru-based vacancy ordered double perovskite for $Cs_2Ru_mPt_{1-m}X_6$ ($X = Cl^-$ and Br^-). Platinum displays markedly weaker d-d transitions in comparison to ruthenium-based compounds. Since the energy level of Pt-5d orbitals are positioned higher than that of Ru-4d, a decrease in bandgap was observed with high Pt content. Cs_2RuX_6 also demonstrated exceptional stability across a wide pH range, from pH 1 to pH 11, though it is not as stable as Cs_2PtX_6, which maintains stability from pH 1 to pH 14. Partial substitution of Ru^{4+} with Pt^{4+} enhanced the photoelectrochemical (PEC) performance of these materials, achieving a higher PEC water oxidation current at Ru^{4+}: Pt^{4+} = 1:1 compared to the pure phases. This improvement is due to a combined effect, where reduced charge-transfer resistance to the electrolyte and increased photovoltage boost PEC performance.

3 | APPLICATIONS AND PERSPECTIVE OF Pt HALIDE PEROVSKITES

3.1 | Single-junction perovskite solar cells

The primary obstacle hindering the commercial viability of lead-based perovskite solar cells is their toxicity and poor stability. In light of these concerns, Pt halide perovskites emerge as promising alternatives due to their non-toxicity and remarkable stability. Our research group has pioneered the experimental synthesis of Cs_2PtI_6 halide double perovskite.[17] Featuring an absorption coefficient of $4 \times 10^5\ cm^{-1}$ ($h\nu > 1.5$ eV) and holes lifetime over 2 μs, the material exhibits a low defect density coupled with a 1.4 eV bandgap that aligns well with the Shockley-Queisser limit.[47] We developed solar cells in F:SnO_2/CdS/Cs_2PtI_6/carbon/Cu configuration with ethylenediamine (EDA) for passivating, yielded promising power conversion efficiency (PCE) of 13.88%. The EDA treatment demonstrated enhanced carrier lifetimes, which in turn contributed to improved device fill factors (FF) through enhanced carrier collection. The solar cell exhibits a high open-circuit voltage (V_{OC}) of 1.07 V with the additive EDA, along with a short-circuit current density J_{SC} of 20 mA/cm^2. This results in a maximum external quantum efficiency (EQE) of 65%.[17] Planar Cs_2PtI_6 devices exhibit low V_{OC}-deficit and no hysteresis in both forward and reverse scans, indicating low trap densities. Cs_2PtI_6 devices showed a decrease in fill factor and open-circuit voltage after 500 h at AM1.5G and 65°C due to device shunting. After our initial attempt, further experimental and simulation studies have been conducted on Pt halide perovskite-based solar cells. Yang et al.[22] reported their fabrication of Cs_2PtI_6 solar cells, employing a conventional planar heterojunction structure comprising ITO/SnO_2/Cs_2PtI_6/Spiro-OMeTAD/Au. The device exhibits a PCE of 0.72%, accompanied by V_{OC} of 0.73 V, J_{SC} of 1.2 mA/cm^2, and FF of 0.82.[22] The observed lower performance has been attributed to the co-presence of Pt^0, indirect bandgap, and suboptimal film quality are also proposed.

Additional simulation studies have evaluated the photovoltaic properties of Cs_2PtI_6. Shamna et al. conducted a comprehensive study of Cs_2PtI_6 based perovskite solar cell using solar cell capacitance simulator one-dimensional (SCAPS-1D) for different electron transport layers (ETLs), hole transport layers (HTLs), and metal contacts.[69] The proper selection of a suitable ETL and HTL is necessary for the extraction of charge carriers formed by the photogeneration process to enhance the

TABLE 5 Experimental and theoretical performance of Cs_2PtI_6-based perovskites solar cells.

Device architecture	V_{OC} (V)	J_{SC} (mA/cm^2)	FF (%)	PCE (%)	References
FTO/CdS/Cs_2PtI_6 with EDA/Carbon/Cu	1.07	19.84	65.03	13.88	17
FTO/CdS/Cs_2PtI_6/carbon/Cu	1.20	20.20	41.51	10.06	17
ITO/SnO_2/Cs_2PtI_6/spiro-OMeTAD/Au	0.73	1.2	82.00	0.72	22
FTO/CdS/Cs_2PtI_6/MoO_3/Cu	1.11	20.14	61	13.9	26
FTO/CdS/Cs_2PtI_6/Cu_2O/Cu	1.1	20.4	62	14.2	26
FTO/CdS/Cs_2PtI_6/CuI/Cu	1.12	20.13	60	13.7	26
FTO/ICZSO/Cs_2PtI_6/Cu_2O/C	1.13	22.2	59.2	14.8	26
FTO/ZnSe/Cs_2PtI_6/Cu_2O/C	1.12	22.3	58	14.7	26
FTO/WS_2/Cs_2PtI_6/Cu_2O/C	1.1	28.1	52.4	16.3	26
FTO/WS_2/Cs_2PtI_6/Cs_2O/C	1.3	28.15	61	22.4	26
FTO/SnO_2/Cs_2PtI_6/MoO_3/GO	1.05	26.94	76.99	21.95	27
FTO/SnO_2/Cs_2PtI_6/MoO_3/C	1.12	26.95	78.08	23.52	27
FTO/ZnO/Cs_2PtI_6/MoO_3/Cu	1.39	16.11	75.54	16.85	69
FTO/ZnO/Cs_2PtI_6/MoO_3/C	1.41	16.11	90.01	20.45	69

performance of the solar cell. Using FTO and Cu as the front and back contact material, FTO/ZnO/Cs_2PtI_6/MoO_3/Cu configuration was first predicted to yield the best photovoltaic parameters of $V_{OC} = 1.39$ V, $J_{SC} = 16.11$ mA/cm^2, FF = 75.54%, and PCE = 16.85% with MoO_3 as HTL and ZnO as ETL and optimized parameters. By replace Cu with high work function carbon as back contacts, an improvement in PCE =20.45% was achieved with $V_{OC} = 1.41$, $J_{SC} = 16.11$ and FF = 90.01%. Additionally, a simulation study by Abdelaziz et al. proposed an optimized structure, FTO/WS_2/Cs_2PtI_6 (400 nm)/Cu_2O/Carbon, for Cs_2PtI_6-based perovskite solar cells, achieving a PCE of 22.4%.[26] The structure is also predicted with J_{SC} of 28.15 mA/cm^2, V_{OC} of 1.3 V, and FF of 61%.[26] Amjad et al. further predicted a groundbreaking PCE of 23.52% and QE of 98.9% in *n-i-p* device architecture (FTO/SnO_2/Cs_2PtI_6/MoO_3/C), with $V_{OC} = 1.12$ V, $J_{SC} = 26.95$ mA/cm^2, and FF = 78.08%.[27] The second-optimal configuration with graphene oxide (GO) as back contact (FTO/SnO_2/Cs_2PtI_6/MoO_3/GO) also achieve performance of PCE = 21.95%, $V_{OC} = 1.05$ V, $J_{SC} = 26.94$ mA/cm^2, and FF = 76.99%.[27] These findings provide important theoretical insights for enhancing the performance of Cs_2PtI_6-based solar cells, emphasizing their strong stability. Despite the promise of high PCE and stability, the cost of Cs_2PtX_6 (X = I and Br) is a barrier to commercialization for utility scale PV applications. Alternately applications such as photocatalytic devices, gas sensors, and photovoltaic devices for space and aerospace applications are promising.

Moreover, beyond the fabrication of perovskite solar cells, Cs_2PtI_6 has emerged as a promising additive for enhancing solar cell performance. Yang et al. demonstrated over 23% PCE for lead-based planar perovskite solar cell through bulk heterojunction design, incorporating Cs_2PtI_6 as a multifunctional perovskite modifier.[29] This inclusion significantly improved perovskite crystal quality, leading to notable enhancements in photovoltaic device parameters attributed to reduced recombination and superior film quality. The devices showed champion PCE of 23.56% with V_{OC} of 1.18 V, J_{SC} of 25.17 mA/cm^2 and FF of 79%.[29] The inclusion of Cs_2PtI_6 with high carrier mobility promoted the perovskite crystals growth, reduced trap-assisted recombination at grain boundaries, and improved carrier collection and transport efficiency. Encouragingly, unencapsulated devices also exhibited less than 10% degradation in performance after 2000 h of storage in ambient humidity (∼30%), underscoring the durability of the optimized design. Table 5 shows a comparison of the up-to-date experimental and theoretical performance of Cs_2PtI_6-based perovskites solar cells.

3.2 | Photoelectrochemical (PEC) and photocatalytic application of Pt-based halide perovskite

As discussed in the previous sections, Cs_2PtI_6 offers extensive visible light absorption, suitable CBM and VBM for catalytic processes, efficient charge transfer kinetics, and remarkable stability in aqueous electrolytes across a broad pH range without the necessity for extra protective coatings. The inherent stability enables direct application for water splitting. The water splitting into hydrogen and

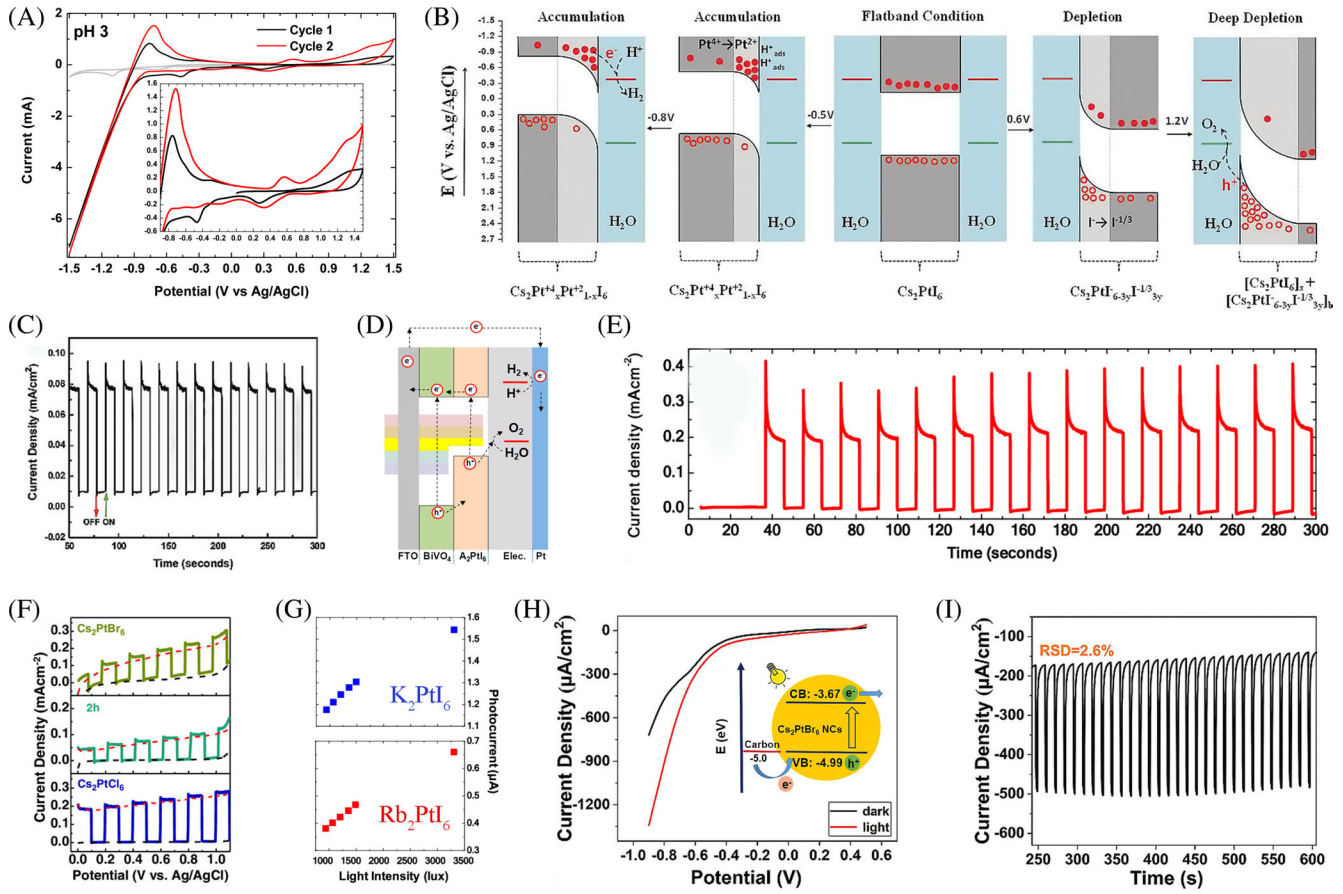

FIGURE 5 Photoelectrochemical (PEC) and photocatalytic application. (A) Cyclic voltammogram of Cs_2PtI_6 recorded at pH 3. (B) Variation in the band edge positions with applied voltage at pH 3. (C) The chopped light measurement of Cs_2PtI_6 at 0.384 V vs. Ag/AgCl confirms the generation of a current that depends on light exposure. The (A)–(C) are reproduced with permission: Copyright 2020, John Wiley and Sons.[20] (D) The PEC device configuration features a tandem photoanode architecture comprising $BiVO_4$ and A_2PtI_6. (E) Chopped light measurements of $BiVO_4/Cs_2PtI_6$ at 0.5 V versus Ag/AgCl (to 1.23 V/RHE). The (D) and (E) are reproduced with permission: 2021, American Chemical Society.[21] (F) Photoelectrochemical (PEC) water oxidation measurements for Cs_2PtCl_6, Cs_2PtBr_6, and core–shell structure formed after 2 h. Reproduced with permission: Copyright 2022, John Wiley and Sons.[19] (G) The Photocurrent of A_2PtI_6 ($A = Cs^+$, Rb^+, and K^+) varies with light intensity, illustrating its response to different levels of illumination. Reproduced with permission: Copyright 2021, American Chemical Society.[21] (H) Line sweep voltammograms plots of perovskite Cs_2PtBr_6 photoanodes. The inset is the diagram of the energy level alignments for Cs_2PtBr_6 NCs. (I) PEC response of the Cs_2PtBr_6 NC/GCE in detection buffer for 30 cycles. The (H) and (I) are reproduced with permission: Copyright 2021, John Wiley and Sons.[23]

oxygen involves two half-reactions: (1) Reduction half-reaction: $2H_2O + 2e^- \rightarrow H_2 + 2OH^-$ (H_2O/H_2, 0 V vs. RHE); (2) Oxidation half-reaction: $2H_2O \rightarrow O_2 + 4H^+ + 4e^-$ (H_2O/O_2, 1.23 V vs. RHE). Muhammed et al. pioneered the utilization of Cs_2PtI_6 as a photoanode on FTO glass for PEC solar water oxidation.[20] Through cyclic voltammetry (CV) measurements in dark conducted in various aqueous solutions ranging from pH 1 to 14, they showed distinct redox processes and stability profiles on the photoanode. At pH 3, upon applying a positive potential bias of approximately 0.6 V (vs. Ag/AgCl), reversible oxidation of iodide (I^-) to triiodide (I_3^-) occurs, forming $Cs_2PtI^-_{6-3y}I^{-1/3}_{3y}$ (Figure 5A). This process causes electron depletion in the conduction band while increasing hole concentration in the valence band at the interface, where the valence band is primarily made up of iodine orbitals in Cs_2PtI_6 (Figure 5B). Subsequently, water oxidation initiates at higher positive biases (e.g., above 1 V vs. Ag/AgCl). Negative bias potentials around −0.46 V (vs. Ag/AgCl) trigger reversible reduction of Pt^{4+} to Pt^{2+}, while higher bias around −0.8 V leads to water reduction. Further scanning down to −1.5 V (vs. Ag/AgCl) results in H^+ reduction to H_2 accompanied by $Pt^{2+} \rightarrow Pt^0$ reduction. Cycling between 0 and − 0.8 V achieved reversible Pt^{2+} /Pt^{4+} conversion, indicating stability in this reduction regime. At pH 13 and 14, suppression of I^- oxidation at positive potentials and reduced Pt^{4+}/Pt^{2+} reduction was observed, prompting the authors to conduct PEC

water oxidation using the n-type Cs_2PtI_6 as a photoanode at pH 11. Cs_2PtI_6 demonstrated a photocurrent of 0.8 mA/cm^2 at 1.23 V (vs. RHE, 0.384 V vs. Ag/AgCl) under simulated AM 1.5G sunlight, the system demonstrated over 12 h of PEC stability, maintaining consistent performance without degradation during constant voltage tests (Figure 5C). Subsequently, this research team further enhanced PEC water oxidation by developing a $Cs_2PtI_6/BiVO_4$ heterojunction as a photoanode (Figure 5D),[21] achieving elevated photocurrent densities without the need for moisture barrier. With Pt as a counter photocathode, at 1.23 V (vs. RHE) and pH 9, bare $BiVO_4$ exhibited a photocurrent density of 0.6 mA/cm^2, whereas the $BiVO_4/Cs_2PtI_6$ heterojunction photoanode demonstrated 0.92 mA/cm^2. Introduction of an IrO_x co-catalyst resulted in an increase in photocurrent density to 2 mA/cm^2 at 1.23 V (vs. RHE). Comparatively, pure $BiVO_4$ required a 560 mV overpotential to achieve 2 mA/cm^2, while the $BiVO_4/Cs_2PtI_6$ heterojunction required only 250 mV overpotential for the same photocurrent density. This improvement in photocurrent stems from enhanced charge separation efficiency from $BiVO_4$ to Cs_2PtI_6, facilitated by appropriate band alignment and complementary absorption characteristics. Chronoamperometric (CA) measurements performed at 0.5 V vs. Ag/AgCl (to 1.23 V vs. RHE) in electrolyte at pH 9, alongside chopped light measurements, showed dynamic photocurrent responses. When the shutter was opened, the photocurrent rapidly increased and then quickly stabilized at 0.2 mA/cm^2 within 1 s. This transient fluctuation may be attributed to the limited influx of reactants to the surface of Cs_2PtI_6 during the oxidation (Figure 5E). The constant current remained around 0.2 mA/cm^2 during the 300 s run of multiple shutter open/close cycles.

Additionally, beyond Cs_2PtI_6, attempts were made with Cs_2PtCl_6 and Cs_2PtBr_6 as photoanodes for solar water oxidation.[19] Electrochemical stability was shown to improve from Cs_2PtI_6 to Cs_2PtCl_6, based on the onset of oxidation peak in CV measurements. PEC water oxidation experiments were conducted on Cs_2PtBr_6, Cs_2PtCl_6, and Cs_2PtCl_6/Cs_2PtBr_6 core–shell systems at pH of 11. Notably, at 0.384 V versus Ag/AgCl (1.23 V vs. RHE) and one sun illumination intensity, Cs_2PtCl_6 displayed a photocurrent density of 0.21 mA/cm^2, while Cs_2PtBr_6 exhibited a photocurrent density of 0.12 mA/cm^2. Long-term PEC stability was assessed for Cs_2PtCl_6, Cs_2PtBr_6, and Cs_2PtI_6 using chronoamperometry at 0.384 V versus Ag/AgCl (to 1.23 V vs. RHE) over 2 h. Cs_2PtCl_6 and Cs_2PtI_6 maintained a current density of 0.16 mA/cm^2, while Cs_2PtBr_6 retained 0.1 mA/cm^2 (Figure 5F). Dark current measurements conducted over 5 min showed a current density below 1 μA/cm^2, which is markedly lower than the photocurrent density. Moreover, Rb_2PtI_6 and K_2PtI_6 exhibited a moderate photocurrent response at 0.75 V (vs. Ag/AgCl), with CV studies indicating redox processes involving I^-/I_3^- halides and platinum (Pt^0) with minimal influence from the A site (Figure 5G).

In contrast to serving as a photoanode, Peng et al.[23] explored the utilization of Cs_2PtBr_6 perovskite nanocrystals as a photocathode, with platinum wire as the counter electrode. Upon illumination, the Cs_2PtBr_6-modified glassy carbon electrode (GCE) exhibited an immediate increase in current, whereas positive potentials caused minimal change in photocurrent, contrasting sharply with the drastically enhanced photo-response observed with negative biases (Figure 5H). However, further negative potentials to deeper region (e.g., over −0.8 V) resulted in irreversible Pt^0 formation, leading to material degradation, akin to findings by Muhammad et al. To safeguard material integrity, a −0.6 V bias-potential was applied. At pH 8, Cs_2PtBr_6 NC/GCE produced a pronounced cathodic photocurrent at −0.6 V Ag/AgCl, achieving a current density of 335 μA/cm^2 when irradiated with 365–370 nm light at intensity of 10.18 mW/cm^2. The repeatability and stability of the PEC system was evaluated by analyzing the consistent photocurrent response during repeated light on/off cycling. The Cs_2PtBr_6 NCs electrode maintained stable performance over 30 cycles, demonstrating its operational stability under illumination.

Anticipated advancements in Cs_2PtX_6 perovskite-based water splitting photoelectrodes and devices offer promising avenues for future research. Key areas of exploration include: (1) Refine the membrane preparation process to ensure secure adhesion and improve charge transport efficiency. (2) Modified halide substitution to tailor material electronic properties and enhance stability through precise precursor mixing. (3) Co-catalyst integration, such as Pt doping, to augment catalytic activity by optimizing reactant adsorption (e.g., H_{ad}) and improving charge carrier separation and transfer dynamics. (4) Modulation of both n-type and p-type semiconductors to fine-tune device performance and efficiency. (5) Optimization of the entire system, encompassing both photoanode and photocathode, and elucidating their interactions (e.g., formation of Z-scheme) to maximize overall efficiency while ensuring efficient H_2 and O_2 separation. These research directions underscore the multifaceted nature of advancing perovskite-based water splitting technologies, offering exciting opportunities for innovation and progress in the field.

3.3 | Pt-based halide perovskite thermoelectric devices

Conversion of waste heat into electrical energy is important for waste heat recovery and sustainable energy

generation.[70,71] Efficient thermoelectric materials with high ZT figure of merit are essential for effectively harnessing this waste heat. To optimize the thermoelectric figure of merit (ZT), a material should have a high Seebeck coefficient (S), high electrical conductivity (σ), and low thermal conductivity (κ) according to the formula $ZT = \frac{S^2\sigma T}{\kappa}$.[30] Recently many lead-free halide double perovskites, including Rb_2NaCoX_6 (X = I, Br, and Cl),[72] $(CH_3NH_3)_2AgInCl_6$,[73] (Na_2AgSbX_6) (X = I, Br, and Cl),[74] $(CH_3NH_3)_2AgLnBr_6$,[75] and X_6SOA_2 (X = Na, K; A = Cl, Br, and I),[76,77] have been indicated as effective thermoelectric materials and potential candidates for thermal energy storage and harvesting. Besides these materials, theoretical studies have identified the extraordinarily stable vacancy-ordered double perovskite Cs_2PtI_6 is also a promising thermoelectric material. In vacancy-ordered perovskites, the absence of polyhedral connectivity enables higher degrees of freedom, causing lattice anharmonicity. Previous discussions have noted substantial charge sharing between Pt—I bonds, attributed to their small electronegativity difference, which indicates covalent bonding. In contrast, Cs does not exhibit charge sharing with Pt or I, suggesting a purely physical interaction with [PtI_6] octahedra. As a result, the electron density around Cs and I is not spherical, contributing to the phonon anharmonicity.[30] The anharmonic lattice dynamics enhance electron–phonon coupling, as electrons interact with lattice vibrations through polarons formation. Cs_2PtI_6 exhibits significant anharmonicity, coupled with low group velocities and high phonon scattering rates (attributed to heavy atoms acting as phonon scatterers), resulting in ultralow lattice thermal conductivity of 0.15 W/mK at 300 K.[30] The computed average thermoelectric figure of merit (ZT) of 0.88,[25] and 1.03,[30] respectively, underscores its promising applications in energy harvesting. The next crucial step involves translating these findings into real-world applications through experimental studies and the fabrication of thermoelectrical devices for waste thermal energy harvesting.

3.4 | Gas sensor based on Pt halide perovskite

In recent years, research on perovskite materials has expanded beyond the realms of solar cells and optics, also garnering increasing attention in the field of gas sensing. Halide perovskites, in particular, have demonstrated remarkable capabilities in detecting various substances at room temperature, including nitrogen dioxide, acetone, ammonia, oxygen, ethanol, hydrogen sulfide, and so on,[78–82] with promising detection limits and selectivity. Cs_2PtI_6 represents a pioneering application of halide perovskites for nitrogen dioxide sensing.[18] It was revealed that NO binds to Pt^{4+} via Pt—N bonds at the I-vacancy site, resulting from the interaction between Pt 5s and N 2s with a high adsorption energy (0.72 eV). Additionally, Pt 5d electron back-donation to N 2px and N 2pz antibonding orbitals, with 0.22 charge transferred from Pt to NO, induces the conductivity change enabling sensing. At 400 ppb NO, noteworthy properties include a response time of 130s and a recovery time within 315s under N_2 purging, comparable to benchmark NO sensors. The longer recovery time reflects the moderate binding strength of NO, leading to slow desorption at room temperature. It is also indicated that a faster recovery could be achieved by increasing the sensing working temperature to 60°C.[18] Thermal stability tests at 10, 30, 50, and 60°C indicate no degradation in response intensity, with accelerated desorption at higher temperatures contributing to decreased response times. Remarkably, the device demonstrates extremely high selectivity for NO at 10 ppm compared to ammonia, carbon dioxide, sulfur dioxide and various volatile organic compounds at the same concentration.[18] With a detection concentration of NO as low as 100 ppb, Cs_2PtI_6 surpasses most traditional meatal oxide materials. Moreover, the NO sensor demonstrates long-term stability, maintaining performance over a span of 60 days across varying NO concentrations, with no discernible changes in film crystallinity or stoichiometry before and after sensing.

4 | 2D Pt(II) HALIDE PEROVSKITE AND INTERSYSTEM CROSSING FOR TRIPLET EXCITON GENERATION

Platinum halide perovskites represent a fascinating avenue for eco-friendly alternative to lead-halide perovskites, offering notable characteristics such as solution processability and stability. Theoretical analyses reveal the inherent instability of pristine 3D $APtX_3$ (A = MA, Cs; X = Cl, Br, I, Pt in $^{2+}$ oxidation state) due to limitations imposed by lattice parameters including factors such as Goldschmidt tolerance factor (e.g., $t = 0.912$ for $CsPtI_3$), Bartel tolerance factor ($\tau = 4.586$ for $CsPtI_3$), and the factor of octahedra ($\mu = 0.364$ for $CsPtI_3$). Empirical observations indicate the optimal parameters for 3D perovskite (ABX_3) lies within the range of $0.8 < t < 0.9$, $0.442 < \mu < 0.895$, and $\tau < 4.18$.[34,83] Consequently, recent research efforts have predominantly centered on double vacancy halide perovskites like Cs_2PtI_6 and its analogues, where Pt is in 4+ oxidation state.

Compared to their 3D counterparts, reducing structural dimensionality (to 2D or 0D) often leads to improvements in environmental stability and significant

alterations in bandgap, band dispersion, and exciton bind energy, and so on. These effects stem from the change in lattice connectivity and quantum confinement experienced by charge carriers in lower-dimensional structures.[84,85]

Recently we reported our progress on the synthesis and characterization of the 2D $CsPtI_3$(DMSO) perovskite phase,[51] which exhibits unique and promising features. Notably, 2D-$CsPtI_3$(DMSO) circumvents the lattice tolerance factor limitations observed in 3D $APtX_3$ perovskites, stabilizing the material in the Pt (II) state rather than the Pt(IV) state found in A_2PtX_6 compounds. Uniform 2D $CsPtI_3$(DMSO) thin film was fabricated with 1.3 μm in thickness. XRD patterns suggest a lamellar structure with well-defined periodic lattice spacing of 8.3 Å, while UV–Vis spectra exhibits an exciton-like feature peak near the absorption edge of 600 nm, due to quantum confinement effects. Further analysis of photoluminescence spectra unveils two distinct emission peaks: a weak emission around 610 nm attributed to singlet exciton recombination and an intense emission around 850 nm resulting from triplet exciton decay via ISC and singlet-to-triplet energy transfer. Moreover, FTIR spectroscopy highlights Pt—S coordination, facilitating rapid intersystem crossing of excitons. ISC and singlet-to-triplet energy transfer indicated the potential application of 2D $CsPtI_3$(DMSO) for room temperature phosphorescence or triplet-triplet annihilation (TTA) based up-conversion devices.[86–88] Additionally, our investigation delves into the thermal or laser induced phase transition of 2D $CsPtI_3$(DMSO) to mixed phase of Cs_2PtI_6/Pt, that holds great potential for designing novel structures in photocatalysis applications.

5 | CONCLUSION

Platinum halide perovskites, particularly Cs_2PtI_6 and its derivatives, hold immense potential across various applications due to their stability, efficiency, and versatility. Continued research and development efforts are needed to optimize their performance and scalability, exploring new avenues for utilization in sustainable technology and scientific discovery. The successful synthesis and characterization of Cs_2PtI_6 and its derivatives have paved the way for their practical applications, showcasing their ability to address critical challenges in renewable energy generation, environmental monitoring, thermoelectric power generation and more. The cost of Pt is a challenge for utility and residential photovoltaics, but applications such as power generation in space, defense and aerospace applications, radiation tolerant electronics, gas sensing, and photocatalytic and thermoelectric devices are promising. We also postulate that modification of structural dimensionality can enable new search of Pb-free halide perovskites with unique optoelectronic properties for stable tandem solar cells.

AUTHOR CONTRIBUTIONS

H. L. and S.B. conceived and conducted the investigation. H.L. wrote the first draft. S.B. supervised the project and provided critical revisions. H. L. and S. B. finalized and approved the manuscript.

ACKNOWLEDGMENTS

This work was supported by the NSF CAREER award [2046944].

CONFLICT OF INTEREST STATEMENT

The authors declare no conflict of interest.

ORCID

Huilong Liu https://orcid.org/0000-0003-3897-8103

REFERENCES

1. Li X, Wu Y, Zhang S, et al. $CsPbX_3$ quantum dots for lighting and displays: room-temperature synthesis, photoluminescence superiorities, underlying origins and white light-emitting diodes. *Adv Funct Mater*. 2016;26(15):2435-2445. doi:10.1002/adfm.201600109
2. Brandt RE, Poindexter JR, Gorai P, et al. Searching for "defect-tolerant" photovoltaic materials: combined theoretical and experimental screening. *Chem Mater*. 2017;29(11):4667-4674. doi:10.1021/acs.chemmater.6b05496
3. Dey A, Ye J, De A, et al. State of the art and prospects for halide perovskite nanocrystals. *ACS Nano*. 2021;15(7):10775-10981. doi:10.1021/acsnano.0c08903
4. Liu C, Cheng YB, Ge Z. Understanding of perovskite crystal growth and film formation in scalable deposition processes. *Chem Soc Rev*. 2020;49(6):1653-1687. doi:10.1039/C9CS00711C
5. Marques AS, Faria RM, Freitas JN, Nogueira AF. Low-temperature blade-coated perovskite solar cells. *Ind Eng Chem Res*. 2021;60(19):7145-7154. doi:10.1021/acs.iecr.1c00789
6. Ye J, Byranvand MM, Martínez CO, Hoye RLZ, Saliba M, Polavarapu L. Defect passivation in Lead-halide perovskite nanocrystals and thin films: toward efficient LEDs and solar cells. *Angew Chem Int Ed*. 2021;60(40):21636-21660. doi:10.1002/anie.202102360
7. Liu H, Bansal S. Metal halide perovskite nanostructures and quantum dots for photocatalytic CO_2 reduction: prospects and challenges. *Mater Today Energy*. 2023;32:32. doi:10.1016/j.mtener.2022.101230
8. Pan S, Li J, Wen Z, et al. Halide perovskite materials for photo(electro)chemical applications: dimensionality, heterojunction, and performance. *Adv Energy Mater Published Online*. 2021;12(4):1-38. doi:10.1002/aenm.202004002
9. Clinckemalie L, Valli D, Roeffaers MBJ, Hofkens J, Pradhan B, Debroye E. Challenges and opportunities for CsPbBr3Perovskites in low- and high-energy radiation detection. *ACS Energy Lett*. 2021;6(4):1290-1314. doi:10.1021/acsenergylett.1c00007
10. Chowdhury TA, Bin Zafar MA, Sajjad-Ul Islam M, Shahinuzzaman M, Islam MA, Khandaker MU. Stability of

perovskite solar cells: issues and prospects. *RSC Adv*. 2023; 13(3):1787-1810. doi:10.1039/D2RA05903G

11. Wu P, Wang S, Li X, Zhang F. Beyond efficiency fever: preventing lead leakage for perovskite solar cells. *Matter*. 2022;5(4): 1137-1161. doi:10.1016/j.matt.2022.02.012
12. Li J, Cao HL, Bin JW, et al. Biological impact of lead from halide perovskites reveals the risk of introducing a safe threshold. *Nat Commun*. 2020;11(1):310. doi:10.1038/s41467-019-13910-y
13. Collin MS, Venkatraman SK, Vijayakumar N, et al. Bioaccumulation of lead (Pb) and its effects on human: a review. *J Hazard Mater Adv*. 2022;7:7. doi:10.1016/j.hazadv.2022.100094
14. Wali Q, Iftikhar FJ, Khan ME, Ullah A, Iqbal Y, Jose R. Advances in stability of perovskite solar cells. *Org Electron*. 2020;78:78. doi:10.1016/j.orgel.2019.105590
15. Fan Q, Biesold-McGee GV, Ma J, et al. Lead-free halide perovskite nanocrystals: crystal structures, synthesis, stabilities, and optical properties. *Angew Chem Int Ed*. 2020;59(3):1030-1046. doi:10.1002/anie.201904862
16. Ghosh S, Pradhan B. Lead-free metal halide perovskite nanocrystals: challenges, applications, and future aspects. *ChemNanoMat*. 2019;5(3):300-312. doi:10.1002/cnma.201800645
17. Schwartz D, Murshed R, Larson H, et al. Air stable, high-efficiency, Pt-based halide perovskite solar cells with long carrier lifetimes. *Phys Status Solidi Rapid Res Lett*. 2020;14(8): 202000182. doi:10.1002/pssr.202000182
18. Chen ZK, Ye W, Lin HZ, Yu C, He JH, Lu JM. Lead-free halide Cs_2PtI_6 perovskite favoring Pt–N bonding for trace NO detection. *ACS Sens*. 2021;6(10):3800-3807. doi:10.1021/acssensors.1c01791
19. Hamdan M, Manoj M, Halpati JS, Chandiran AK. Acid- and base-stable Cs2Pt(Cl,Br)6Vacancy-ordered double perovskites and their core–shell heterostructures for solar water oxidation. *Solar RRL*. 2022;6(7):2101092. doi:10.1002/solr.202101092
20. Hamdan M, Chandiran AK. Cs_2PtI_6 halide perovskite is stable to air, moisture, and extreme pH: application to Photoelectrochemical solar water oxidation. *Angew Chem Int Ed*. 2020; 59(37):16033-16038. doi:10.1002/anie.202000175
21. Jayaraman JP, Hamdan M, Velpula M, Kaisare NS, Chandiran AK. $BiVO_4/Cs_2PtI_6$ vacancy-ordered halide perovskite heterojunction for panchromatic light harvesting and enhanced charge separation in Photoelectrochemical water oxidation. *ACS Appl Mater Interfaces*. 2021;13(14):16267-16278. doi:10.1021/acsami.0c22654
22. Yang S, Wang L, Zhao S, et al. Novel Lead-free material Cs_2PtI_6 with narrow bandgap and ultra-stability for its photovoltaic application. *ACS Appl Mater Interfaces*. 2020;12(40):44700-44709. doi:10.1021/acsami.0c11429
23. Peng H, Xu L, Sheng Y, et al. Highly conductive ligand-free Cs2PtBr6 Perovskite nanocrystals with a narrow bandgap and efficient Photoelectrochemical performance. *Small*. 2021; 17(38):2102149. doi:10.1002/smll.202102149
24. Suzuki S, Tsuyama M. Structural, electronic, and optical properties of Pt-based vacancy-ordered double perovskites A_2PtX_6 (a = K, Rb, Cs; X = Cl, Br, I) in tetragonal P4/mnc polymorph. *Opt Mater (Amst)*. 2021;119:111323. doi:10.1016/j.optmat.2021.111323
25. Bhumla P, Jain M, Sheoran S, Bhattacharya S. Vacancy-ordered double perovskites Cs_2BI_6(B = Pt, Pd, Te, Sn): an emerging class of thermoelectric materials. *J Phys Chem Lett*. 2022; 13(50):11655-11662. doi:10.1021/acs.jpclett.2c02852
26. AbdElAziz HH, Taha M, El Rouby WMA, Khedr MH, Saad L. Evaluating the performance of $Cs_2PtI_{6-x}Br_x$ for photovoltaic and photocatalytic applications using first-principles study and SCAPS-1D simulation. *Heliyon*. 2022;8(10):e10808. doi:10.1016/j.heliyon.2022.e10808
27. Amjad A, Qamar S, Zhao C, Fatima K, Sultan M, Akhter Z. Numerical simulation of lead-free vacancy ordered Cs_2PtI_6 based perovskite solar cell using SCAPS-1D. *RSC Adv*. 2023; 13(33):23211-23222. doi:10.1039/D3RA04176J
28. Tang T, Diao X, Tang Y. Optoelectronic property tuning of A_2BX_6(A = In, Tl; B = Pd, Pt; X = Cl, Br, I): a first-principles study. *Chem Phys Lett*. 2023;826:140678. doi:10.1016/j.cplett.2023.140678
29. Yang S, Han Q, Wang L, et al. Over 23% power conversion efficiency of planar perovskite solar cells via bulk heterojunction design. *Chem Eng J*. 2021;426:131838. doi:10.1016/j.cej.2021.131838
30. Sajjad M, Mahmood Q, Singh N, Larsson JA. Ultralow lattice thermal conductivity in double perovskite Cs_2PtI_6: a promising thermoelectric material. *ACS Appl Energy Mater*. 2020;3(11): 11293-11299. doi:10.1021/acsaem.0c02236
31. Ye X, Liu A, Zhao Y, Han Q, Kitamura T, Ma T. DFT study of X-site ion substitution doping of Cs_2PtX_6 on its structural and electronic properties. *Int J Energy Res*. 2022;46(6):8471-8479. doi:10.1002/er.7696
32. Ye X, Liu A, Gao L, et al. Computational screening of Cs based vacancy-ordered double perovskites for solar cell and photocatalysis applications. *EcoMat*. 2023;5(3):e12295. doi:10.1002/eom2.12295
33. Goldschmidt VM. Die Gesetze der Krystallochemie. *Naturwissenschaften*. 1926;14(21):477-485. doi:10.1007/BF01507527
34. Bartel CJ, Sutton C, Goldsmith BR, et al. New tolerance factor to predict the stability of perovskite oxides and halides. *Sci Adv*. 2019;5(2):eaav0693. doi:10.1126/sciadv.aav0693
35. Babayigit A, Ethirajan A, Muller M, Conings B. Toxicity of organometal halide perovskite solar cells. *Nat Mater*. 2016; 15(3):247-251. doi:10.1038/nmat4572
36. Debnath T, Kim E, Lee K, Nath NCD. Halide perovskite solar cells with biocompatibility. *Adv Energy Sustain Res*. 2020;1(1): 2000028. doi:10.1002/aesr.202000028
37. Sinitsyna O, Paralikar P, Pandit R, Rai M. Platinum in biomedical applications. *Biomedical Applications of Metals*. Springer International Publishing; 2018:151-165. doi:10.1007/978-3-319-74814-6_7
38. Samhitha SS, Surabhi S, Saireddy SK, Santhosh G. Platinum nanoparticles in biomedical applications: antibacterial and antiviral perspectives. In: Kokkarachedu V, Sadiku R, eds. *Nanoparticles in Modern Antimicrobial and Antiviral Applications. Nanotechnology in the Life Sciences*. Cham: Springer; 2024:47-64. doi:10.1007/978-3-031-50093-0_3
39. Shinde S, Hamdan M, Bhalla P, Chandiran AK. Biocompatible Cs_2PtX_6 (X = Cl, Br, I) vacancy ordered perovskites and *Shewanella oneidensis* MR-1 bacteria hybrid for potential photocatalytic solar fuel production. *ACS Eng Au*. 2024;4(2):224-230. doi:10.1021/acsengineeringau.3c00061
40. Thiele G, Mrozek C, Kämmerer D, Wittmann K. On Hexaiodoplatinates(IV) M_2PtI_6 (M = K, Rb, Cs, NH_4, Tl)

-preparation, properties and structural data. *Z Naturforsch*. 1983;38(8):905-910. doi:10.1515/znb-1983-0802

41. Sa R, Luo B, Ma Z, Liu D. The effect of the A-site cation on the stability and physical properties of vacancy-ordered double perovskites A_2PtI_6 (a = Tl, K, Rb, and Cs). *J Solid State Chem*. 2022;305:122714. doi:10.1016/j.jssc.2021.122714
42. Ito S. Research update: overview of progress about efficiency and stability on perovskite solar cells. *APL Mater*. 2016;4(9): 091504. doi:10.1063/1.4961955
43. Leijtens T, Bush K, Cheacharoen R, Beal R, Bowring A, McGehee MD. Towards enabling stable lead halide perovskite solar cells; interplay between structural, environmental, and thermal stability. *J Mater Chem A Mater*. 2017;5(23):11483-11500. doi:10.1039/C7TA00434F
44. Sheikh AD, Bera A, Haque MA, et al. Atmospheric effects on the photovoltaic performance of hybrid perovskite solar cells. *Solar Energy Mater Solar Cells*. 2015;137:6-14. doi:10.1016/j.solmat.2015.01.023
45. Yang J, Siempelkamp BD, Liu D, Kelly TL. Investigation of $CH_3NH_3PbI_3$ degradation rates and mechanisms in controlled humidity environments using in situ techniques. *ACS Nano*. 2015;9(2):1955-1963. doi:10.1021/nn506864k
46. Deeth RJ, Jenkins HDB. A density functional and thermochemical study of M−X bond lengths and energies in $[MX_6]^{2-}$ complexes: LDA versus Becke88/Perdew86 gradient-corrected Functionals. *J Phys Chem A*. 1997;101(26):4793-4798. doi:10.1021/jp970374n
47. Rühle S. Tabulated values of the Shockley–Queisser limit for single junction solar cells. *Solar Energy*. 2016;130:139-147. doi:10.1016/j.solener.2016.02.015
48. Umebayashi T, Asai K, Kondo T, Nakao A. Electronic structures of lead iodide based low-dimensional crystals. *Phys Rev B*. 2003;67(15):155405. doi:10.1103/PhysRevB.67.155405
49. Sa R, Zhang Q, Luo B, Liu D. Exploring the electronic and optical properties of vacancy-ordered double perovskites Cs_2PtX_6(X = Cl, Br, I). *J Solid State Chem*. 2021;304:122602. doi:10.1016/j.jssc.2021.122602
50. Zhang W, Xia S, Chen C, et al. Understanding the crucial roles of catalyst properties in ethyl acetate and toluene oxidation over Pt catalysts. *New J Chem*. 2021;45(25):11352-11358. doi:10.1039/D1NJ01823J
51. Liu H, Biswas M, Walter S, et al. Stabilizing 2D Pt-based halide perovskites via solvent lone pair donation. *Authorea*. 2024. doi:10.22541/au.172526264.42273909/v1 (Submitted to Advanced Optical Materials, in progress).
52. Guo X, Li J, Wang Y, Rui Z. Photothermocatalytic water splitting over Pt/$ZnIn_2S_4$ for hydrogen production without external heat. *Catal Today*. 2022;402:210-219. doi:10.1016/j.cattod.2022.04.001
53. Wang S, Lu A, Zhong CJ. Hydrogen production from water electrolysis: role of catalysts. *Nano Converg*. 2021;8(1):4. doi:10.1186/s40580-021-00254-x
54. Zhou P, Chen H, Chao Y, et al. Single-atom Pt-I_3 sites on all-inorganic Cs_2SnI_6 perovskite for efficient photocatalytic hydrogen production. *Nat Commun*. 2021;12(1):4412. doi:10.1038/s41467-021-24702-8
55. Phani Chandra NV, Hamdan M, Chandiran AK. Stable Cs_2ReX_6 (X – Cl, Br) vacancy-ordered perovskites for solar water splitting. *Sustain Energy Fuels*. 2023;7(4):949-955. doi:10.1039/D2SE01281B
56. Saura-Múzquiz M, Avdeev M, Brand HEA, Kennedy BJ. Structural and magnetic properties of some vacancy-ordered osmium halide perovskites. *Inorg Chem*. 2022;61(40):15961-15972. doi:10.1021/acs.inorgchem.2c02171
57. Shanmugam N, Halpati JS, Chandiran AK. Highly stable and panchromatic light absorbing Cs_2OsX_6 (X = Cl^-, Br^-, I^-) vacancy ordered perovskites as Photoanodes for solar water oxidation. *Adv Mater Interfaces*. 2023;10(2):2201526. doi:10.1002/admi.202201526
58. Zhou L, Liao JF, Huang ZG, et al. All-inorganic Lead-free Cs_2PdX_6 (X = Br, I) perovskite nanocrystals with single unit cell thickness and high stability. *ACS Energy Lett*. 2018;3(10): 2613-2619. doi:10.1021/acsenergylett.8b01770
59. Scholz M, Morgenroth M, Merker A, Oum K, Lenzer T. Ultrafast carrier dynamics and electrical properties of the palladium-based vacancy-ordered perovskite Cs_2PdBr_6. *J Phys Chem C*. 2023;127(36):17871-17879. doi:10.1021/acs.jpcc.3c04001
60. Sakai N, Haghighirad AA, Filip MR, et al. Solution-processed cesium hexabromopalladate(IV), Cs2PdBr6, for optoelectronic applications. *J Am Chem Soc*. 2017;139(17):6030-6033. doi:10.1021/jacs.6b13258
61. Halpati JS, Shanmugam N, Manoj M, Hamdan M, Chandiran AK. Mixed-tetravalent Cs_2 $Ru_mPt_{1-m}X_6$(X = Cl^-, Br^-)-based vacancy-ordered halide double perovskites for enhanced solar water oxidation. *Solar RRL*. 2024;8(5):2300924. doi:10.1002/solr.202300924
62. Chang T, Wei Q, Zeng R, Cao S, Zhao J, Zou B. Efficient energy transfer in Te^{4+} -doped Cs_2ZrCl_6 vacancy-ordered perovskites and ultrahigh moisture stability via A-site Rb-alloying strategy. *J Phys Chem Lett*. 2021;12(7):1829-1837. doi:10.1021/acs.jpclett.1c00255
63. Sun J, Zheng W, Huang P, et al. Efficient near-infrared luminescence in lanthanide-doped vacancy-ordered double perovskite Cs_2ZrCl_6 phosphors via Te^{4+} sensitization. *Angew Chem Int Ed*. 2022;61(26):e202201933. doi:10.1002/anie.202201993
64. Bryan PS, Ferranti SA. Luminescence of Cs_2ZrCl_6 and Cs_2HfCl_6. *JOL*. 1984;31-32(1):117-119. doi:10.1016/0022-2313(84)90220-5
65. Liu S, Yang B, Chen J, et al. Efficient thermally activated delayed fluorescence from all-inorganic cesium zirconium halide perovskite nanocrystals. *Angew Chem Int Ed*. 2020; 59(49):21925-21929. doi:10.1002/anie.202009101
66. Xiong G, Yuan L, Jin Y, et al. Aliovalent doping and surface grafting enable efficient and stable Lead-free blue-emitting perovskite derivative. *Adv Opt Mater*. 2020;8(20):2000779. doi:10.1002/adom.202000779
67. Li S, Luo J, Liu J, Tang J. Self-trapped Excitons in all-inorganic halide perovskites: fundamentals, status, and potential applications. *J Phys Chem Lett*. 2019;10(8):1999-2007. doi:10.1021/acs.jpclett.8b03604
68. Stamokostas GL, Fiete GA. Mixing of t_{2g}-e_g orbitals in 4d and 5d transition metal oxides. *Phys Rev B*. 2018;97(8):85150. doi:10.1103/PhysRevB.97.085150
69. Shamna MS, Sudheer KS. Device modeling of Cs_2PtI_6-based perovskite solar cell with diverse transport materials and contact metal electrodes: a comprehensive simulation study using

solar cell capacitance simulator. *J Photonics Energy*. 2022;12(3): 032211. doi:10.1117/1.JPE.12.032211
70. Tan G, Zhao LD, Kanatzidis MG. Rationally designing high-performance bulk thermoelectric materials. *Chem Rev*. 2016; 116(19):12123-12149. doi:10.1021/acs.chemrev.6b00255
71. Mukhopadhyay S, Reinecke TL. Lone-pair electron-driven Thermoelectrics at room temperature. *J Phys Chem Lett*. 2019; 10(14):4117-4122. doi:10.1021/acs.jpclett.9b01625
72. Kumari S, Rani U, Rani M, et al. Computational investigation of the fundamental physical properties of lead-free halide double perovskite Rb_2NaCoX_6 (X = Cl, Br, and I) materials: potential prospects for sustainable energy. *Mod Phys Lett B*. 2024;9. doi:10.1142/S0217984924503238
73. Rani U, Kamlesh PK, Singh R, et al. Exploring properties of organometallic double perovskite $(CH_3NH_3)_2AgInCl_6$: a novel material for energy conversion devices. *Mod Phys Lett B*. 2024; 38(18):2450144. doi:10.1142/S0217984924501446
74. Kumari S, Kamlesh PK, Kumari L, et al. Progress in theoretical study of lead-free halide double perovskite Na_2AgSbX_6 (X = F, Cl, Br, and I) thermoelectric materials. *J Mol Model*. 2023; 29(6):195. doi:10.1007/s00894-023-05599-0
75. Rani U, Kamlesh PK, Agrawal R, Shukla A, Singh VA. Emerging study on Lead-free hybrid double perovskite $(CH_3NH_3)_2AgInBr_6$: potential material for energy conversion between heat and electricity. *Energy Dent Tech*. 2022;10(9): 202200002. doi:10.1002/ente.202200002
76. Rani U, Soni Y, Kamlesh PK, Pachori S, Verma AS. Fundamental theoretical design of Na-ion and K-ion based double antiperovskite X_6SOA_2 (X = Na, K; a = Cl, Br and I) halides: potential candidate for energy storage and harvester. *Int J Energy Res*. 2021;45(9):13442-13460. doi:10.1002/er.6673
77. Rani U, Kamlesh PK, Agarwal R, Kumari J, Verma AS. Electronic and thermo-physical properties of double antiperovskites X_6SOA_2 (X = Na, K and a = Cl, Br, I): a non-toxic and efficient energy storage materials. *Int J Quantum Chem*. 2021;121(19): e26759. doi:10.1002/qua.26759
78. Fu X, Jiao S, Dong N, et al. A $CH_3NH_3PbI_3$ film for a room-temperature NO_2 gas sensor with quick response and high selectivity. *RSC Adv*. 2018;8(1):390-395. doi:10.1039/C7RA11149E
79. Chen H, Zhang M, Bo R, et al. Superior self-powered room-temperature chemical sensing with light-activated inorganic halides perovskites. *Small*. 2018;14(7):1702571. doi:10.1002/smll.201702571
80. Sheikh AD, Vhanalakar V, Katware A, Pawar K, Patil PS. Two-step antisolvent precipitated $MAPbI_3$-pellet-based robust room-temperature ammonia sensor. *Adv Mater Technol*. 2019;4(9): 1900251.
81. Zhang H, Yi J. Enhanced ethanol gas sensing performance of ZnO nanoflowers decorated with $LaMnO_3$ perovskite nanoparticles. *Mater Lett*. 2018;216:196-198. doi:10.1016/j.matlet.2018.01.018
82. Balamurugan C, Lee DW. Perovskite hexagonal $YMnO_3$ nanopowder as p-type semiconductor gas sensor for H_2S detection. *Sens Actuat B Chem*. 2015;221:857-866. doi:10.1016/j.snb.2015.07.018
83. Cortecchia D, Dewi HA, Yin J, et al. Lead-free $MA_2CuCl_xBr_{4-x}$ hybrid perovskites. *Inorg Chem*. 2016;55(3):1044-1052. doi:10.1021/acs.inorgchem.5b01896
84. Hoye RLZ, Hidalgo J, Jagt RA, Correa-Baena J, Fix T, MacManus-Driscoll JL. The role of dimensionality on the optoelectronic properties of oxide and halide perovskites, and their halide derivatives. *Adv Energy Mater*. 2022;12(4):2100499. doi:10.1002/aenm.202100499
85. Mao L, Stoumpos CC, Kanatzidis MG. Two-dimensional hybrid halide perovskites: principles and promises. *J Am Chem Soc*. 2019;141(3):1171-1190. doi:10.1021/jacs.8b10851
86. Sullivan CM, Nienhaus L. Generating spin-triplet states at the bulk perovskite/organic interface for photon upconversion. *Nanoscale*. 2023;15(3):998-1013. doi:10.1039/D2NR05767K
87. VanOrman ZA, Drozdick HK, Wieghold S, Nienhaus L. Bulk halide perovskites as triplet sensitizers: progress and prospects in photon upconversion. *J Mater Chem C Mater*. 2021;9(8): 2685-2694. doi:10.1039/D1TC00245G
88. Younts R, Duan H, Gautam B, et al. Efficient generation of long-lived triplet Excitons in 2D hybrid perovskite. *Adv Mater*. 2017;29(9). doi:10.1002/adma.201604278
89. Engel G. Die Kristallstrukturen einiger hexachlorokomplexsalze. *Z Kristallogr Cryst Mater*. 1935;90(1–6):341-373. doi:10.1524/zkri.1935.90.1.341

AUTHOR BIOGRAPHIES

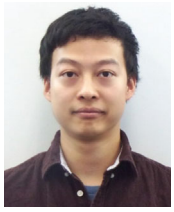

Huilong Liu joined Purdue as a Ph. D. student in Mechanical Engineering in Spring 2023 and his research focuses on development of low-dimensional (2D, Nanoparticles, Quantum Dots) lead-free halide perovskites. Huilong obtained his B.S. from Huazhong University of Science and Technology (China) in Biomedical Engineering and M.S. from Chongqing Medical University (China).

Shubhra Bansal is an Associate Professor at Purdue University with a joint appointment in School of Mechanical Engineering and School of Materials Engineering. She holds B.Tech. degree in Metallurgical and Materials Engineering (2001)) from the Indian Institute of Technology, Roorkee. She received her M.S. (2003) and Ph.D. (2006) in Materials Science and Engineering from Georgia Institute of Technology, focusing on development of nanocrystalline Cu-pillar chip-to-package interconnects at the pioneering GT-PRC with Prof. Rao Tummala. Her professional career began at GE Global Research (2006–2011) following which, she served as a Senior Technical Advisor for President Obama's SunShot Initiative at the Department of Energy (2011–2015). Prior to joining Purdue in 2023, Dr. Bansal was an Associate Professor in Mechanical Engineering at University

of Nevada Las Vegas (2015–2022). Among others, Dr. Bansal received 2010 GE Outstanding Individual Achievement Award, 2014 U.S. Department of Energy Technical Excellence Award, 2020 UNLV Faculty Excellence Award, 2021 NSF CAREER Award, 2021 DOE Faculty Fellowship, and 2022 NASA Glenn Faculty Fellowship. Her research interests include novel materials, reliability and sustainability for renewable energy and semiconductor packaging applications. She is a senior member of IEEE, and currently serves as the Associate Editor of IEEE- Journal of Photovoltaics and Elsevier Solar Energy Journal.

How to cite this article: Liu H, Bansal S. Pt and Pt-group transition metal 0D vacancy ordered halide perovskites: A review. *EcoMat*. 2024;6(11): e12492. doi:10.1002/eom2.12492